arXiv:1704.02656v1 [physics.flu-dyn] 9 Apr 2017

Effect of free-surface on submerged stratified shear instabilities

MIHIR H. SHETE[1] AND ANIRBAN GUHA[1]†

[1] Environmental and Geophysical Fluids Group, Department of Mechanical Engineering, Indian Institute of Technology, Kanpur, U.P. 208016, India.

(Received ?? and in revised form ??)

In this paper we have considered the effects of shallowness of the domain as well as air-water free-surface on the stratified shear instabilities of the fluid below. First we numerically solve the non-Boussinesq Taylor-Goldstein equation for smooth velocity and density profiles of a model shear layer with a free-surface. When the depth of the fluid is relatively shallow, the surface gravity waves existing at the free-surface come closer to the shear layer. This can lead to resonant interactions between the surface waves and the waves present in the stratified shear layer. In order to obtain a deeper understanding of the instability mechanisms, we have performed analytical studies with broken-line profiles. Furthermore, reduced order broken-line profiles have also been developed, based on which dispersion diagrams are constructed. Through these diagrams we have underpinned the resonantly interacting waves leading to each type of instability. Two new instabilities have been found - one of them arises due to the interaction between a surface gravity wave and an interfacial gravity wave (SGIG). The other one, which arises due to the interaction between a surface gravity wave and the lower vorticity wave (SGLV), surpasses the Kelvin-Helmholtz instability (KH) to become the most unstable mode of the system. Stability boundary of the SGLV mode is found to be quite different from that of KH. In fact KH becomes negligible for very shallow flows, while SGLV's growth rate is significant - comparable to the growth rate of KH for unbounded domains (≈ 0.18). Moreover, the SGLV mode is found to be analogous to the barotropic mode observed in two layered quiescent flows. The effect of free-surface on the Holmboe instability is not appreciable. Holmboe in presence of a free-surface is found to be analogous to the baroclinic mode observed in two layered quiescent flows. When the free-surface is replaced by a rigid-lid, remarkable differences are observed when the domain is shallow. We infer that rigid-lid approximation is valid for large domain extents and should be applied with caution otherwise.

1. Introduction

Flows in natural environment like lakes, estuaries and oceans are shallow, density stratified and furthermore, exhibit a free surface. In presence of a background velocity shear, which may arise due to wind forcing, exchange flow (due to horizontal thermal or salinity gradients), etc., it is possible for a stable density stratified flow to become unstable. The resulting instabilities are known as stratified shear instabilities, and a few well known examples are Kelvin-Helmholtz instability (KH), Holmboe instability, and Taylor-Caulfield (TC) instability. These instabilities are often observed in the pycnocline region (sharp density changes due to salinity, temperature, or both) in natural flows.

† Electronic mail for correspondence: anirbanguha.ubc@gmail.com

Instabilities cause the interfacial gravity waves present in the pycnocline to grow and break, which often leads to intense turbulent mixing, and thereby profoundly affects the aquatic environment.

Shear instabilities arising in the environment have been conventionally studied in an infinite vertical extent of the background fluid. Here the effect of the free-surface (interface between air and water) is neglected, hence Boussinesq approximation can be effectively applied. Boussinesq approximation neglects the effect of density variation in the inertial terms, but considers it in the buoyancy term (Turner 1979). This approximation gives accurate results *only* when the density differences are small compared to the mean background density (for example, slight density differences between warm (fresh) and cold (salty) waters). However, Boussinesq approximation will not hold if the effect of the free-surface (i.e. large density difference between air and water) is taken into account.

There have been numerous studies on linear stability analyses and direct numerical simulations of Boussinesq stratified shear instabilities, e.g. Smyth *et al.* (1988), Smyth & Peltier (1989), Smyth & Peltier (1991), Lawrence *et al.* (1991), Sutherland & Peltier (1992), Alexakis (2005), Carpenter *et al.* (2007), Smyth *et al.* (2007), Carpenter *et al.* (2010), Guha *et al.* (2013) and Rahmani *et al.* (2014). These studies have modeled the free-surface as a rigid-lid, and furthermore, they have considered very large domain extent as compared to the shear layer thickness (to emulate an infinite domain). An important step towards considering the flows in natural environment is to see the effect of shallowness by taking into account the finite extent of vertical domain, while still using Boussinesq approximation (by assuming the free-surface to be a rigid-lid). Hazel (1972) and Haigh & Lawrence (1999) have shown that the presence of rigid-lid close to the shear layer significantly affects the stability characteristics. Furthermore, there have been few studies which have considered the effect of free-surface on submerged shear instabilities (Longuet-Higgins 1998; Bakas & Ioannou 2009). Here the fluid below is homogeneous, and the domain extends up to the free-surface (so there is technically no fluid above the free-surface). While these studies do incorporate the effect of surface waves on submerged KH/Rayleigh instability, the free-surface modeling is an approximate one (meaning, non-Boussinesq effects have not been considered). Since the free-surface is indeed non-Boussinesq, it needs to be modeled carefully. The correct equations for a non-Boussinesq interface have been outlined in Barros & Choi (2011), and Heifetz & Mak (2015).

The importance of free-surface is more than just a boundary condition. The free-surface supports surface gravity waves. These waves can interact with the different vorticity and interfacial gravity waves that are supported in the stratified shear layer. A schematic provided in figure 1 shows that there are six waves in the system, two surface gravity waves (marked by 1 and 2), two interfacial gravity waves at the pycnocline (marked by 4 and 5), and two vorticity waves, one at each vorticity jump (marked by 3 and 6). The mean flow profile of a shear layer Doppler shifts different waves differently (at least some of them). A growing body of literature provides a conceptual understanding of shear instabilities in terms of resonant interaction at a distance between counter-propagating (each wave's intrinsic phase speed is opposite to the local mean flow, and, for the case of two waves, the intrinsic phase speed of the waves are opposite) waves (Holmboe 1962; Sakai 1989; Baines & Mitsudera 1994; Caulfield 1994; Heifetz *et al.* 1999; Heifetz & Methven 2005; Carpenter *et al.* 2013; Guha & Lawrence 2014). Classic KH (or Rayleigh) instability will result via an interaction between waves $3-6$ of figure 1, while classic Holmboe will be due to $3-4$ and/or $5-6$. Likewise, the surface gravity waves can also resonantly interact with (at least) one of the waves existing in the submerged shear layer. Intuitively we can expect two additional interactions simply by searching

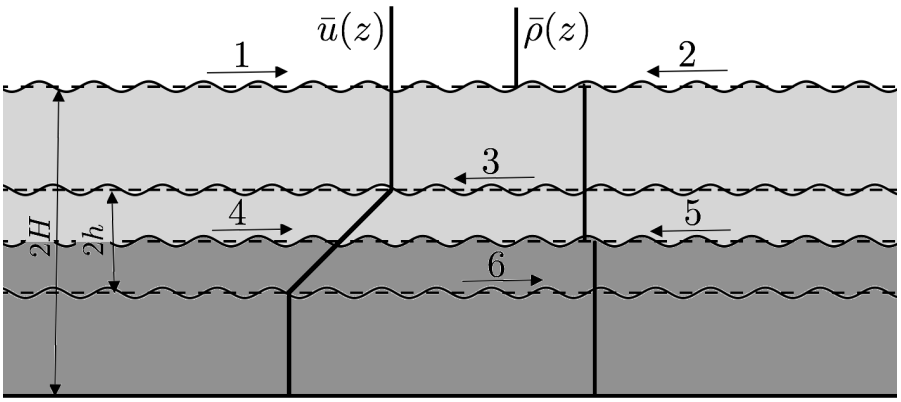

Figure 1: Schematic of a two-layered stratified shear layer in presence of a free-surface. Light gray color indicates lighter while dark gray color indicates heavier fluid. Each arrow with a number indicates the wave present at that location, arrow giving the direction of the intrinsic phase speed.

for counter-propagating configurations: $2-4$, surface gravity interacting with interfacial gravity (SGIG) and $2-6$, surface gravity interacting with lower vorticity (SGLV). In this paper we will explore whether these instabilities are actually possible. Intuitively, we can also expect the interactions to be more prominent if the free-surface is not very far from the pycnocline.

The objective of the present study is to consider the effects of shallowness and the free-surface on the stratified shear instabilities of the fluid below. The pycnocline is assumed to be sharp, so as to capture both KH and Holmboe modes. In natural settings, the free surface in many occasions is not far from the pycnocline. Furthermore, natural flows being mostly shallow, one can expect a non-trivial effect of the free-surface on the instabilities occurring inside the fluid. While studying stratified shear instabilities in Ishikari River estuary Yoshida *et al.* (1998) observed KH and Holmboe at the interface (pycnocline) when there is no wind. However in presence of wind the situation is very different - "When the wind blows, gravity waves often arise to destroy the interface. The details of the complicated mechanisms of this transformation remain undescribed, however, as do those responsible for transport of salt to the surface once the interface is gone". Shete & Guha (2016) have analyzed the effect of free-surface on the stability of base profiles prevalent in density stratified two-layered lakes undergoing double circulation. For the broad shear profile prevalent in lakes a new instability arising due to the interaction of surface vorticity gravity wave and interfacial gravity wave was observed.

The paper is organized as follows. In §2 we outline the fundamental equations describing the flow physics, specifically the non-Boussinesq Taylor-Goldstein equation. We also briefly state numerical procedure to solve this eigenvalue problem. In §3 we discuss the smooth base state profiles and perform the numerical stability analyses. The broken-line profile corresponding to the continuous profile, which is required for providing a mechanistic understanding of the instabilities identified in §3, is discussed in §4. Reduced order broken-line profiles are also devised to single out the key waves that lead to some newly discovered instability mechanisms. The understanding of these mechanisms are augmented by studying the dispersion diagrams. Finally, discussions and conclusions are stated in §5.

2. Governing equations and eigenvalue problem

2.1. *Governing equations*

We model the density stratified shear layer using the 2D incompressible and inviscid Navier-Stokes equations along with the mass continuity equation. The flow is in the x-z plane with the density stratification along the vertical (z) axis. The horizontal and vertical components of velocity are respectively u and w. To accurately model the free-surface we use a non-Boussinesq model. The model takes into account the effect of inhomogeneity of density in the inertia terms under the purview of linear approximation. A good way to understand the effect of density inhomogeneity is to examine the vorticity equation. The vorticity equation for a 2D density stratified fluid is given by:

$$\frac{\partial q}{\partial t} + u\frac{\partial q}{\partial x} + w\frac{\partial q}{\partial z} = \frac{1}{\rho^2}\Big(\frac{\partial \rho}{\partial z}\frac{\partial p}{\partial x} - \frac{\partial \rho}{\partial x}\frac{\partial p}{\partial z}\Big), \tag{2.1}$$

Here vorticity is given by $q \equiv \partial u/\partial z - \partial w/\partial x$, while ρ, p and g denote density, pressure and acceleration due to gravity respectively. The terms on the right hand side of (2.1) denote the baroclinic generation of vorticity. A base state that varies only along z is assumed. The base state is given by $u = \bar{u}(z)$, $w = 0$, $\bar{q}(z) = d\bar{u}/dz$, $p = \bar{p}(z)$ and $\rho = \bar{\rho}(z)$. The base state follows hydrostatic pressure balance $d\bar{p}/dz = -\bar{\rho}g$. Perturbations are added to the base flow: $u = \bar{u}(z) + \tilde{u}$, $w = \tilde{w}$, $p = \bar{p}(z) + \tilde{p}$, $\rho = \bar{\rho}(z) + \tilde{\rho}$, and $q = \bar{q}(z) + \tilde{q}$, where $\tilde{f}$ denotes the perturbation quantities (f is a placeholder variable). We assume the perturbations to be infinitesimal and linearize (2.1). This results in the perturbation vorticity evolution equation and is given by:

$$\frac{\partial \tilde{q}}{\partial t} + \bar{u}\frac{\partial \tilde{q}}{\partial x} = -\tilde{w}\frac{d\bar{q}}{dz} + \frac{g}{\bar{\rho}}\frac{\partial \tilde{\rho}}{\partial x} + \frac{1}{\bar{\rho}^2}\Big(\frac{d\bar{\rho}}{dz}\frac{\partial \tilde{p}}{\partial x}\Big), \tag{2.2}$$

The same equation can also be found in Heifetz & Mak (2015) (their equation (5)). The first term on the right hand side of (2.2) given by

$$-\tilde{w}\frac{d\bar{q}}{dz}$$

denotes the barotropic generation of vorticity, and arises due to the advection of base state vorticity gradient by the vertical velocity. The second term on the right hand side of (2.2), given by

$$\frac{g}{\bar{\rho}}\frac{\partial \tilde{\rho}}{\partial x},$$

denotes the Boussinesq baroclinic generation of vorticity. Boussinesq baroclinic torque is responsible for the propagation of interfacial gravity waves at the pycnocline. A point to note here is that the Boussinesq baroclinic torque is also present in the non-Boussinesq regime. We have named it "Boussinesq" because it is the only baroclinic generation term present when the Boussinesq approximation is invoked.

The last term on the right hand side of (2.2) given by

$$T_3 \equiv \frac{1}{\bar{\rho}^2}\Big(\frac{d\bar{\rho}}{dz}\frac{\partial \tilde{p}}{\partial x}\Big),$$

is the non-Boussinesq baroclinic generation of vorticity. This term (hereafter, we refer to it as T_3) is absent in the Boussinesq model, since the Boussinesq approximation (Turner 1979) neglects density variation in all terms except the buoyancy term. However, even for modeling the free-surface (the highly non-Boussinesq interface between air and water), T_3 has been neglected in Bakas & Ioannou (2009) (see their equation (6)) as well as

Longuet-Higgins (1998) (they do not explicitly write in terms of the vorticity equation). The question whether ignoring T_3 is always reasonable will be addressed in §3.2.

2.2. *The non-Boussinesq Taylor-Goldstein equation*

We now present the non-Boussinesq Taylor-Goldstein equation in the inviscid and non-diffusive limit. To obtain it we assume temporal normal mode form for the perturbations given by $\tilde{f} = \hat{f}(z)\mathrm{e}^{\mathrm{i}\alpha(x-ct)}$. Here α and c are respectively the real wavenumber and the complex phase speed ($c = c_r + \mathrm{i}c_i$), and f could represent u, w, p, q or ρ. Temporal normal mode form is substituted in the linearized Navier-Stokes equations, yielding

$$\bar{\rho}'\Big[(\bar{u}-c)\hat{w}' - \bar{u}'\hat{w} - \frac{g}{\bar{u}-c}\hat{w}\Big] + \bar{\rho}\Big[(\bar{u}-c)(\hat{w}'' - \alpha^2\hat{w}) - \bar{u}''\hat{w}\Big] = 0. \tag{2.3}$$

Total derivative with respect to z is denoted by $'$. A complete derivation of the above equation can be found in Appendix A. The non-Boussinesq Taylor-Goldstein equation obtained is similar to the one obtained by Barros & Choi (2011), Barros & Choi (2014), Carpenter *et al.* (Accepted) and Shete & Guha (2016). We intend to solve (2.3) for smooth profiles of base state velocity and density, and for this numerical eigenvalue solver is necessary. The numerical solution of (2.3) poses a resolution issue. A very fine spacing in parameter space is required, this raises the computational cost tremendously. An efficient way to control the resolution issue is to introduce numerical viscosity and diffusivity, respectively given by μ and κ. Hence we numerically solve the viscous diffusive form of the non-Boussinesq Taylor-Goldstein, which is given by:

$$\bar{\rho}'[-(\bar{u}-c)\hat{w}' + \bar{u}'\hat{w}] + \bar{\rho}[-(\bar{u}-c)\hat{w}'' + \alpha^2(\bar{u}-c)\hat{w} + \bar{u}''\hat{w}] = \mathrm{i}\alpha\hat{\rho}g + \frac{\mathrm{i}}{\alpha}\mu[\hat{w}'''' - 2\alpha^2\hat{w}'' + \alpha^4\hat{w}], \tag{2.4}$$

$$\mathrm{i}\alpha(\bar{u}-c)\hat{\rho} + \hat{w}\bar{\rho}' = \kappa(\hat{\rho}'' - \alpha^2\hat{\rho}). \tag{2.5}$$

A complete derivation of (2.4) and (2.5) is provided in Appendix A. Equations (2.4) and (2.5) form a system of simultaneous equations for the eigenfunctions $\hat{w}$ and $\hat{\rho}$ and the eigenvalue c. Note that the first two term in (2.4) containing $\bar{\rho}'$ are the non-Boussinesq terms and are absent in the corresponding Boussinesq equations. The viscous diffusive non-Boussinesq Taylor-Goldstein equation is similar to Shete & Guha (2016). The Boussinesq limit equation can be found in the appendix of Smyth *et al.* (2011). In the next subsection we describe in brief the numerical strategy to solve the eigenvalue problem.

2.3. *Solution of the eigenvalue problem*

Equations (2.4) and (2.5) can be converted into the form of a generalized eigenvalue problem of the form $M\boldsymbol{\vartheta} = cN\boldsymbol{\vartheta}$:

$$\begin{bmatrix} M_{11} & M_{12} \\ M_{21} & M_{22} \end{bmatrix} \begin{bmatrix} \vartheta_1 \\ \vartheta_2 \end{bmatrix} = c \begin{bmatrix} N_{11} & N_{12} \\ N_{21} & N_{22} \end{bmatrix} \begin{bmatrix} \vartheta_1 \\ \vartheta_2 \end{bmatrix}. \tag{2.6}$$

Elements of the matrices are given by

$$M_{11} = \bar{\rho}'[-\bar{u}D + \bar{u}'] + \bar{\rho}[-\bar{u}D^2 + \alpha^2\bar{u} + \bar{u}''] - \frac{\mathrm{i}}{\alpha}\mu[D^4 - 2\alpha^2D^2 + \alpha^4],$$

$$M_{12} = -\mathrm{i}\alpha g, \quad M_{21} = \bar{\rho}', \quad M_{22} = \mathrm{i}\alpha\bar{u} - \kappa[D^2 - \alpha^2], \quad \vartheta_1 = \hat{w}, \quad \vartheta_2 = \hat{\rho},$$

$$N_{11} = -\bar{\rho}'D + \bar{\rho}[-D^2 + \alpha^2], \quad N_{12} = 0, \quad N_{21} = 0, \quad N_{22} = \mathrm{i}\alpha.$$

Equation (2.6) is an eigenvalue problem for eigenvalue c and eigenfunctions $\hat{w}$ and $\hat{\rho}$. D, D^2 and D^4 are the first, second and fourth derivative matrices for the total derivatives with respect to z. Fourth order central difference schemes have been used to evaluate

D, D^2 and D^4. Since central differencing is not possible at the boundaries, the boundary points have been discretized using second order one sided finite difference schemes. The boundary conditions used for $\hat{w}$ are impenetrability and free-slip. The impenetrable boundary condition arises due to the continuum hypothesis and is given by,

$$\hat{w} = 0. \tag{2.7}$$

The free-slip boundary condition is given by,

$$\frac{d^2\hat{w}}{dz^2} = 0. \tag{2.8}$$

The boundary condition used for $\hat{\rho}$ is the insulating boundary condition given by,

$$\frac{d\hat{\rho}}{dz} = 0. \tag{2.9}$$

The insulating boundary condition is preferable in cases where there is no physical boundary, since it has minimal effect on flow. Equation (2.6) along with the boundary conditions (2.7)-(2.9) form the matrix eigenvalue problem for the eigenvalues c and the eigenfunctions $\hat{w}$ and $\hat{\rho}$. The matrix eigenvalue problem is solved using built-in functions in MATLAB. The numerical solution procedure used is similar to the one used by Smyth *et al.* (2011) and Shete & Guha (2016). The numerical routine developed has been validated against the Boussinesq shear layer problem of Smyth *et al.* (1988) and that of surface gravity waves. Our primary interest is to capture inviscid instabilities like KH and Holmboe, hence viscosity (μ) and diffusivity (κ) introduced in (2.4) and (2.5) are treated as purely numerical parameters for controlling the resolution issue. The stability characteristics do not vary appreciably on changing the numerical parameters by an order of magnitude. We have analyzed the stability of base state velocity and density profiles respectively given in (3.1) and (3.2), and furthermore shown in figure 2.

3. Numerical stability analysis of the smooth profiles

3.1. *Base state profiles*

In order to model a stratified shear layer, we use hyperbolic tangent functions in z to represent the base state velocity and density profiles. Since we are interested in analyzing the effect of the free-surface on the shear layer below, we need to extend the velocity profile in air. This extension has been made such that (i) the velocity profile is continuously differentiable at the free-surface, and (ii) the velocity remains nearly constant with z away from the free-surface. The first point ensures that the derivatives of base state velocity remain finite, which is required for numerical stability of (2.6). The second point ensures avoiding the formation of critical layers in the air region. In other words, we avoid the wind-wave instability of Miles (1957). The dimensional base state velocity variation is given by:

$$\bar{u}(z) = U \tanh\Big(\frac{z}{h} - \frac{h_r}{2}\Big). \tag{3.1}$$

Here U represents the surface current and h is the half shear layer thickness. In this paper we have taken $h = 1/2$. The parameter $h_r = H/h$ quantifies the non-dimensional distance of the free-surface from the center of the shear layer (pycnocline and center of shear layer coincides since we are only analyzing symmetric shear layers). H is the dimensional half-depth of the channel (i.e. distance between free-surface and bottom is $2H$). If h_r is not large, moderately long waves inside the shear layer can feel the effect of the free-surface. In the present study we have detailed the results for $h_r = 10$, 4, 3 and 2.

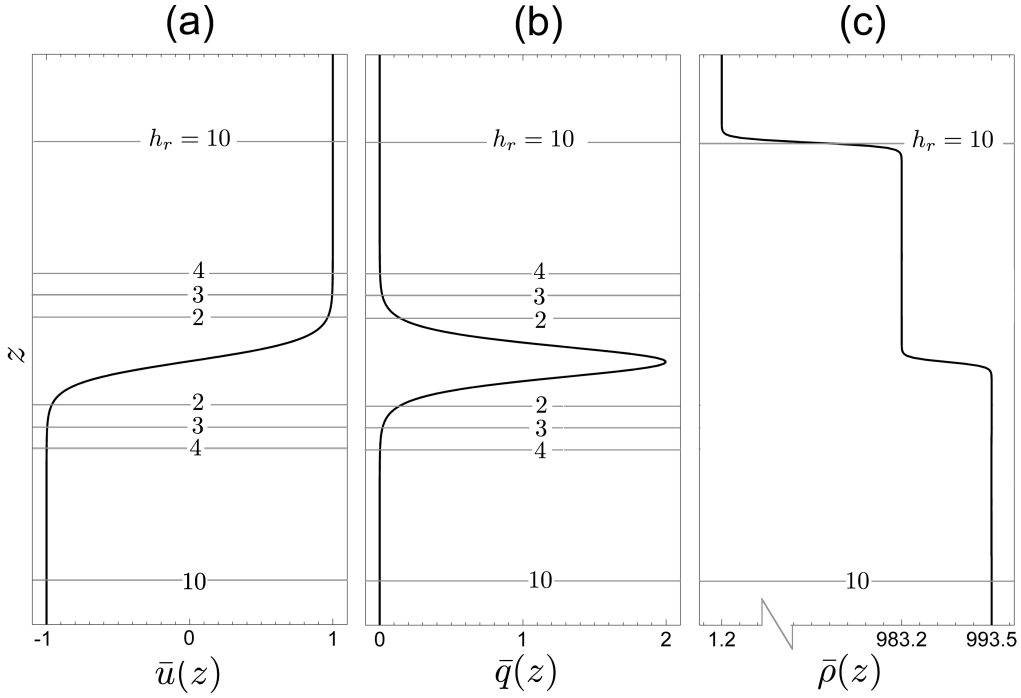

Figure 2: The base state plots for (a) horizontal velocity, $\bar{u}$, corresponding to $U = 1$, (b) corresponding vorticity, $\bar{q}$, and (c) density, $\bar{\rho}$ corresponding to $h_r = 10$ (which indicates the location of the free-surface). The horizontal lines indicate the domain extent of the water body for each h_r. For example, when $h_r = 3$, the vertical domain of the water body is between the horizontal lines indicated by "3" (which means that the free-surface and the bottom boundary will respectively occur at the upper and lower horizontal lines indicated by "3").

These values of h_r have been chosen so that a clear transition in stability characteristics can be seen as the surface gravity waves come closer to the other waves present in the shear layer (therefore getting an opportunity to resonantly interact with them).

The dimensional base state density profile is given by:

$$\bar{\rho}(z) = \begin{cases} 492.2 - 491 \tanh\left(5\Big(\dfrac{z}{h} - h_r\Big)\right) & 1.2h_r \leqslant \dfrac{z}{h} \leqslant 0.75h_r, \\ \\ 988.35 - 5.15 \tanh\left(5\Big(\dfrac{z}{h} - \dfrac{h_r}{2}\Big)\right) & 0.75h_r \leqslant \dfrac{z}{h} \leqslant 0. \end{cases} \tag{3.2}$$

3.2. *The issue with "Boussinesq" free-surface*

As noted in §2.1, a few previous studies (Longuet-Higgins 1998; Bakas & Ioannou 2009) that considered the effect of free-surface on the shear instability below have ignored the term $T_3 \equiv (\bar{\rho})^{-2}(d\bar{\rho}/dz)(\partial\tilde{p}/\partial x)$ appearing in (2.2). For the purpose of comparison we have analyzed the free-surface effect using two different models, namely the "Boussinesq free-surface model" (which ignores T_3) and the "non-Boussinesq free-surface model" (which fully solves (2.2)). Here we try to understand the implications of assuming $T_3 = 0$. There are two possibilities:

(i) $d\bar{\rho}/dz = 0$: This is a valid approximation in the Boussinesq limit (where $\bar{\rho} \approx$

constant). In our setting, T_3 will only matter at the free-surface, where obviously $d\bar{\rho}/dz \neq 0$, but is approximately a delta function. Hence assuming $d\bar{\rho}/dz = 0$ for air-water density jump is not correct.

(ii) $\partial\tilde{p}/\partial x = 0$: In the inviscid limit, $\partial\tilde{p}/\partial x = -\bar{\rho}\mathbb{D}\tilde{u}/\mathbb{D}t$, where $\mathbb{D}/\mathbb{D}t$ is the material derivative; see (A 12). For surface gravity waves, the free-surface is a vortex sheet ($\tilde{u}$ changes sign above and below the free-surface), hence $\tilde{u} = 0$ at the free-surface. This implies $\partial\tilde{p}/\partial x = 0$. In fact, the term T_3 is neglected in obtaining the dispersion relation for surface gravity waves†. However, the above is true *only* when the base shear flow, $\bar{q}$ is absent at the interface. If $\bar{q} \neq 0$ at the interface, then $\partial\tilde{p}/\partial x = -\bar{\rho}\bar{q}\tilde{w} \neq 0$. Furthermore, $\tilde{u}$ may not be 0 at the interface in a more general setting, thus $\mathbb{D}\tilde{u}/\mathbb{D}t$, which implies $\partial\tilde{p}/\partial x$ cannot be neglected in general.

3.3. *Non-dimensionalization and key dimensionless numbers*

Apart from the non-dimensional distance h_r (defined previously), another parameter of key importance is the bulk Richardson number, J, given by

$$J = At\frac{gh}{U^2}. \tag{3.3}$$

Here At is the Atwood number associated with the pycnocline:

$$At = \frac{\rho_{cw} - \rho_{ww}}{\rho_{ww}} = \frac{10.3}{983.2} \approx 0.01. \tag{3.4}$$

The densities of cold water and warm water are respectively given by ρ_{cw} and ρ_{ww}.

For reporting stability characteristics we have non-dimensionalized the wavenumber, α, the phase speed, c, and the growth rate $\Im\{\alpha c\}$. The wavenumber is non-dimensionalized by half shear layer thickness, h, while the phase speed is non-dimensionalized by the surface velocity, U. Growth rates are non-dimensionalized by U/h.

3.4. *Variation of stability characteristics with h_r*

Here we have studied the effect of varying the distance between the free-surface and the pycnocline (i.e. h_r in non-dimensional terms) on the submerged stratified shear layer. As mentioned previously, the proximity between the surface gravity waves and the vorticity and interfacial gravity waves existing in the shear layer can affect the stability characteristics. A comparison of stability characteristics of a stratified shear layer in presence of a rigid-lid, a Boussinesq free-surface, and an actual/non-Boussinesq free-surface for $h_r = 10$ are shown in figures 3(a)-(c). In this case we see a very good match between the rigid-lid and the non-Boussinesq free-surface, which is expected since the free-surface is located quite far. The maximum growth rate and corresponding phase speed also agree very well, as can be seen from table 1. The Boussinesq free-surface, on the other hand, shows some differences in the growth rate contours. This can be prominently seen near $\alpha = 0.25$ and $J = 0.1$. This difference is because of density scaling, and has been discussed in §4.1.

If we look at the first column of figure 3, which corresponds to the rigid-lid case, it becomes clear that decreasing h_r significantly decreases the maximum growth rate. The KH instabilities (the downward pointing closed curves having higher growth rates) are more significantly affected than the Holmboe modes (the upward pointing open curves with lesser growth rates). Moreover, short waves are stabilized by this process, as is

† This is usually done by appealing to the fact that $\tilde{p} = 0$ (atmospheric) at the free-surface $z/h = h_r + \tilde{\eta}$ (where $\tilde{\eta}$ is free-surface displacement), and therefore by linearization, $\tilde{p} = 0$ even at $z = h_r$; see Sutherland (2010).

evident from the leftward shift of the right stability boundary. The results are in good agreement with that of Hazel (1972) and Haigh & Lawrence (1999).

The results obtained on replacing the rigid-lid by a non-Boussinesq free-surface are significantly different; see the last column of figure 3. Decreasing h_r has little effect on the maximum growth rate; see table 1. However, the stability boundaries change quite dramatically, and furthermore, new modes appear. The distinct identity of the KH mode observed for $h_r = 10$ is lost in $h_r = 3$; a part of it separates out as "bubble" and becomes a part of the Holmboe branch. The other part near $J = 0$ axis leads to a new mode, the SGLV mode, which is distinctly visible at $h_r = 3$ and 2. The SGLV mode always has the highest growth rate. Comparing with the rigid-lid case (first column), it can be straightforwardly argued that the SGLV mode wouldn't exist if there were no surface gravity waves. We will show later that the SGLV mode is a result of the interaction between waves $2 - 6$ in figure 1.

The stability characteristics of the Boussinesq free-surface case, as seen from the middle column of figure 3, is intermediate between the rigid-lid case and the non-Boussinesq free-surface case. As discussed previously, in presence of a background shear at the free-surface, these results would physically correspond to the stability of an analogous system where, instead of air, the uppermost fluid is slightly lighter than warm water. In absence of background shear at the free-surface, "Boussinesq free-surface" exactly matches with the "non-Boussinesq free-surface" (which happens, as discussed before, for the $h_r = 10$ case).

3.5. *Understanding unstable modes through eigenfunctions*

The eigenfunction of the perturbation streamfunction, $\hat{\psi}$, can be obtained from the vertical velocity, $\hat{w}$, via the relation $\hat{\psi} = -\mathrm{i}\hat{w}/\alpha$ ($\hat{w}$ is obtained by solving the eigenvalue problem (2.6)). Since eigenfunctions are non-unique, we normalize $\hat{\psi}$ by its maximum value for reporting purposes. Apart from plotting $\hat{\psi}$, we have also plotted the contours of perturbation streamfunction $\tilde{\psi} = \Re\{\hat{\psi}\mathrm{e}^{\mathrm{i}\alpha x}\}$ for one wavelength of the disturbance. The direction of the perturbed velocity field would be tangential to the contour lines. The eigenfunction of the density perturbations, $\hat{\rho}$ is normalized by the maximum value of the corresponding $\hat{\psi}$. The contours of perturbation density, $\tilde{\rho}$ are also plotted for one wavelength. This spatial variation reveals information about the gravity waves present in the system, their relative magnitudes and phases.

3.5.1. *Unstable modes for non-Boussinesq free-surface, $h_r = 10$*

KH mode: To elucidate the role of different waves and their interactions in the system, the perturbed streamfunction and density and their eigenfunction are plotted in figure 4. The mode depicted in figures 4 corresponds to the most unstable mode of the KH instability, given by $(\alpha, J) = (0.4431, 0)$, for the non-Boussinesq free-surface case with $h_r = 10$ (refer to figure 3(c)). Figure 4 shows the classic eigenstructure of KH instability (see Sutherland (2010)) - a critical layer around $z = 5$ where $\bar{u}$ has an infection point, and peaks in $|\hat{\psi}|$ at the two extrema of the base state vorticity gradient, $\bar{q}' = d^2\bar{u}/dz^2$. From the peaks in $|\hat{\psi}|$ it can be inferred that the KH instability arises due to the interaction of two vorticity waves.

Figure 4 shows two peaks in perturbation density, one at the free-surface (signifying surface gravity wave) and the other at the pycnocline (signifying interfacial gravity wave). It is important to note here that this plot corresponds to $J = 0$†, which by definition (see (3.3)) can imply either $At = 0$ (water is unstratified) or $U \to \infty$. We have chosen

† In all the figures corresponding to $J = 0$ we have plotted for a small positive J.

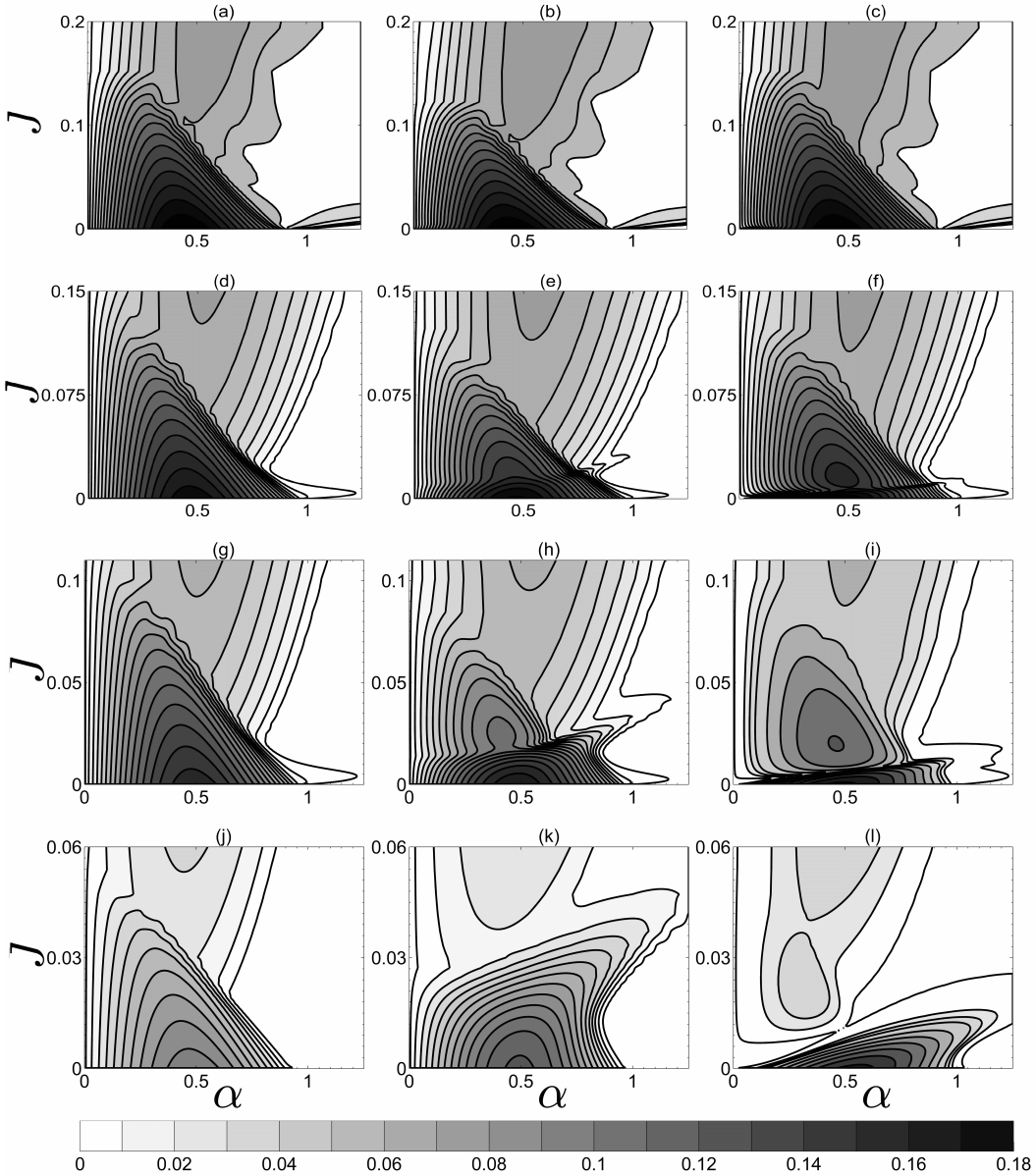

Figure 3: Growth rate contours in the α-J plane for the numerical stability of smooth profiles. Each row represents growth rates for a given h_r. First row: $h_r = 10$, second row: $h_r = 4$, third row: $h_r = 3$, and fourth row: $h_r = 2$. The left, middle and right columns respectively correspond to rigid-lid, Boussinesq free-surface, and non-Boussinesq free-surface.

the second implication (hence $At \neq 0$) in order to show the density perturbation when $J \ll 1$. Furthermore, since Boussinesq approximation is never invoked, the phase speed of the most unstable KH mode is not 0 but -0.0051. Analytically it can be shown that for vortex sheet type KH with two-layered density stratification, where the top fluid is moving with a speed 1 and bottom fluid with -1, the phase speed $c_r = -At$ (see

Case	h_r	Mode	α	J	γ	c_r
Rigid-lid	10	KH	0.4474	0	0.1893	0
	10	H	0.6773	0.3498	0.0781	$\pm$0.4140
	4	KH	0.4724	0	0.1769	0
	4	H	0.6815	0.3498	0.0768	$\pm$0.4155
	3	KH	0.4892	0	0.1566	0
	3	H	0.6898	0.3498	0.0737	$\pm$0.4191
	2	KH	0.4849	0	0.0966	0
	2	H	0.8152	0.5106	0.0618	$\pm$0.4864
Boussinesq free-surface	10	KH	0.4431	0	0.1893	$-$0.0001
	10	H	0.6438	0.2545	0.078	$-$0.3894
	4	SGLV/KH	0.4640	0	0.1815	$-$0.0153
	4	H	0.6522	0.2545	0.0765	$-$0.3912
	3	SGLV	0.4808	0	0.1677	$-$0.0276
	3	KH	0.4139	0.0247	0.1035	$-$0.0038
	3	H	0.7525	0.3498	0.0734	$-$0.4516
	2	SGLV	0.4933	0	0.1224	$-$0.0375
	2	H	0.7818	0.3498	0.0604	$-$0.4590
Non-Boussinesq free-surface	10	KH	0.4431	0	0.1894	$-$0.0051
	10	H	0.6775	0.3498	0.0788	$-$0.4155
	4	SGLV	0.4557	0	0.1884	$-$0.0513
	4	KH	0.46826	0.0152	0.15445	$-$0.00695
	4	H	0.6898	0.3498	0.07708	$-$0.41638
	3	SGLV	0.4808	0	0.1844	$-$0.1010
	3	KH	0.4599	0.019	0.1209	$-$0.0073
	3	H	0.715	0.3498	0.0729	$-$0.4197
	2	SGLV	0.5477	0	0.1658	$-$0.1789
	2	KH	0.3219	0.0227	0.0374	$-$0.0150
	2	H	0.8695	0.5106	0.0569	$-$0.4827

Table 1: Growth rates and phase speeds for the maximum growth rate mode of the smooth profiles. "H" stands for Holmboe. To keep parity in nomenclature, we have refereed even the remnants of KH (in Boussinesq free-surface as well as Non-Boussinesq free-surface cases) as "KH". These modes are strongly affected by surface gravity waves.

Drazin (2002)). Hence if $At \neq 0$, but a small positive number, we get a small negative phase-speed.

Holmboe mode: Holmboe instability results due to the interaction between counter-propagating vorticity waves and interfacial gravity waves. The maximum growth rate mode for Holmboe instability corresponds to $(\alpha, J) = (0.6775, 0.3498)$ in figure 3(c). The corresponding streamfunction and density perturbation contours and eigenfunctions have been plotted in figure 5. The peaks of $|\hat{\psi}|$ occur at the pycnocline (upper peak) and the lower vorticity gradient extremum (lower peak), verifying the fact that Holmboe instability arises due to an interaction between an interfacial gravity wave and a vorticity wave. We should note here that the free-surface introduces a small asymmetry, favouring the "leftward Holmboe mode" over the "rightward Holmboe mode". This is because the leftward propagating vorticity wave (which exists at the upper extrema of base vorticity gradient) being closer to the free-surface gets more affected. Therefore, the leftward propagating Holmboe mode, arising due to the interaction between the rightward propagating vorticity wave and the leftward propagating interfacial gravity wave, becomes the dominant mode of the two Holmboe modes. This leftward propagating mode, with phase

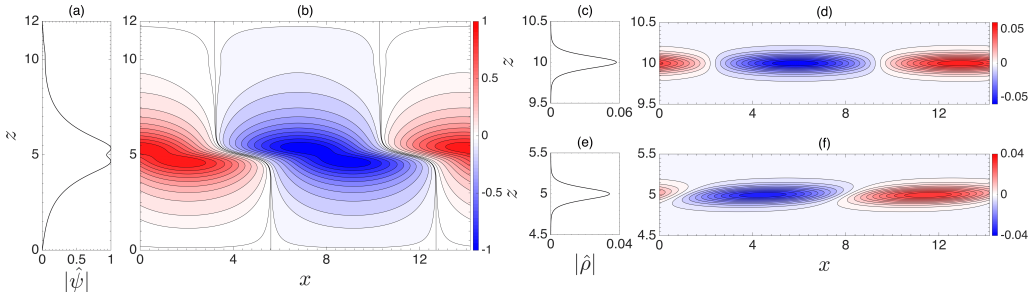

Figure 4: Plots for the perturbation streamfunction and density for the non-Boussinesq free-surface case for $h_r = 10$. The plot corresponds to the maximum growth rate mode of KH instability, given by $(\alpha, J) = (0.4431, 0)$. (a) Norm of the perturbation streamfunction eigenfunction, $\hat{\psi}$ versus z, and (b) contours of the perturbation streamfunction $\tilde{\psi}$. The perturbation density characteristics near the free-surface ($z = 10$): (c) norm of the perturbation density eigenfunction, $\hat{\rho}$ versus z and (d) contours of the perturbation density $\tilde{\rho}$. The perturbation density characteristics near the pycnocline ($z = 5$): (e) norm of the perturbation density eigenfunction, $\hat{\rho}$ versus z and (f) contours of the perturbation density $\tilde{\rho}$.

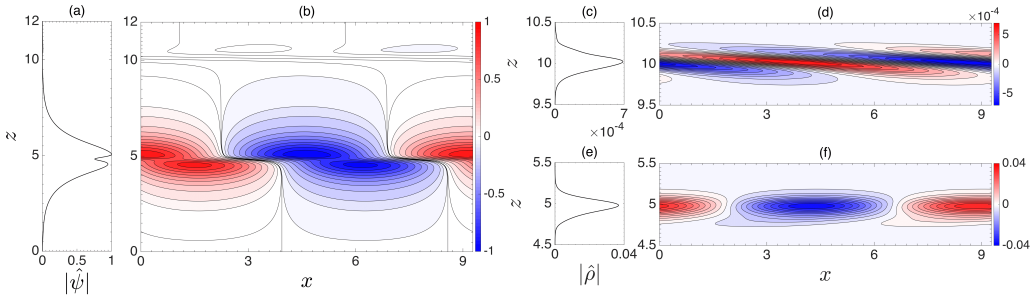

Figure 5: As in figure 4 but for the maximum growth rate mode of the Holmboe instability, given by $(\alpha, J) = (0.6775, 0.3498)$.

speed $c_r = -0.4155$ (see table 1), curves into the lower fluid region, as clearly evidenced in figure 5(f).

A few salient features of Holmboe instability in presence of a free-surface are worth noticing. The value of $\hat{\rho}$ is a few orders of magnitude smaller at the free-surface than that at the interface; see figures 5(c)-(f). The same figures also show that the density contours at the free-surface and the interface are π phase shifted. These two features are the hallmark of the classic "baroclinic/internal mode" in layered flows (in absence of background velocity shear). The analogy of Holmboe instability with baroclinic mode makes sense because, like baroclinic mode, Holmboe instability is driven by the baroclinic torque produced at the interface.

3.5.2. *Unstable modes for non-Boussinesq free-surface, $h_r = 3$*

SGLV mode: The maximum SGLV mode growth rate for $h_r = 3$ is given by $(\alpha, J) = (0.4808, 0)$ (refer to figure 3(i)). The perturbation streamfunction and density are plotted in figure 6. Figures 6(c)-(f) show that $|\hat{\rho}|$ has two peaks, one at the free-surface and the other at the pycnocline, the former being two orders of magnitude greater than the latter. Furthermore, the surface and the interfacial gravity waves are nearly in phase.

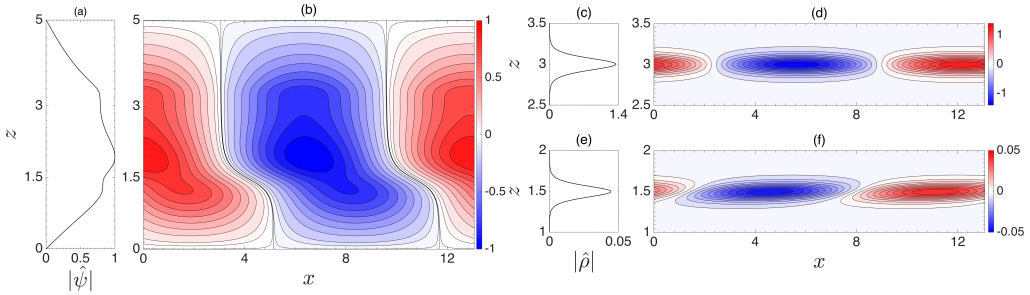

Figure 6: As in figure 4 but for $h_r = 3$. The plot corresponds to the maximum growth rate mode of the SGLV instability, given by $(\alpha, J) = (0.4808, 0)$.

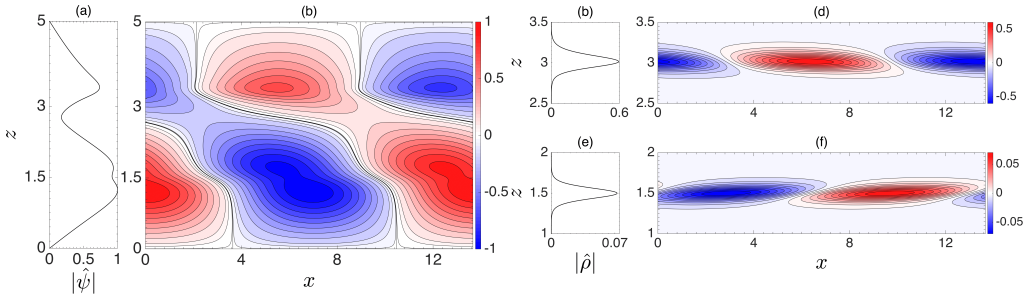

Figure 7: As in figure 4 but for $h_r = 3$. The plot corresponds to the maximum growth rate mode of the separating KH bubble mode, given by $(\alpha, J) = (0.4599, 0.019)$.

This configuration resembles the classic "barotropic/external mode" in layered flows. The interfacial gravity wave plays nearly no role in the instability process. This instability arises due to the resonant interaction between the leftward propagating surface gravity wave and the lower vorticity wave (which is rightward propagating), i.e. waves $2-6$ in figure 1. As evident from table 1, SGLV mode has the highest growth rate for $h_r = 3$, and this growth rate is comparable to KH in a nearly unbounded flow (compare with the growth rate of KH mode for $h_r = 10$). The phase speed of this mode is ≈ -0.1, and is intermediate between KH and Holmboe modes for the same h_r.

Separating KH bubble: Here we investigate the fate of the original KH mode. The maximum growth rate mode for $h_r = 3$ is given by $(\alpha, J) = (0.4599, 0.019)$. In figure 3(i), the stability boundary of this mode appears as distinct closed contours within the outer Holmboe region. As seen from table 1, this mode has a very small phase speed, like classic KH in two-layered flows. The perturbed streamfunction and density are plotted in figure 7. The $|\hat{\psi}|$ plot within the water domain ($0 \leqslant z \leqslant 3$) shows similarity with that of KH in figure 4, with peaks at the two vorticity gradient extrema. The KH here is strongly affected by the surface wave, as evidenced by the high magnitude of $|\hat{\rho}|$ in figure 7(c). Furthermore, figure 7(e) shows that the interfacial gravity wave's effect is negligible.

Holmboe mode: The mode corresponding to the maximum growth rate for the Holmboe instability for $h_r = 3$ is given by $(\alpha, J) = (0.715, 0.3498)$. The perturbed streamfunction and density are shown in figure 8. Qualitatively, the figures are quite similar to the Holmboe mode for $h_r = 10$, except for the smaller peak in $\tilde{\psi}$ in the air region. One thing worth mentioning here is that the surface wave now has become quiet important, and its maximum magnitude is twice that of the interfacial wave. This is not a pure surface

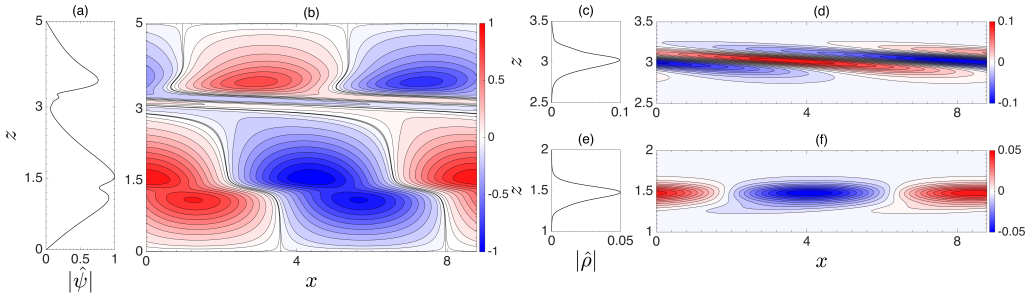

Figure 8: As in figure 4 but for $h_r = 3$. The plot corresponds to the maximum growth rate mode of the Holmboe mode, given by $(\alpha, J) = (0.715, 0.3498)$.

gravity wave but a mixed surface gravity-vorticity wave, as can also be inferred from figure 8(a).

4. Broken-line profiles and mechanistic picture of instability

4.1. *Broken-line profiles and reduced order models*

To complement the stability analyses of smooth profiles outlines in §3, we undertake stability analyses of broken-line profiles in this section. Broken-line profiles are more accurate in underpinning the mechanism of instabilities, as the waves in the system are localized instead of being diffused as is the case for smooth profiles. The broken-line profiles being piecewise linear can be solved analytically using (2.3), which can be converted to an equivalent form given by:

$$\{\bar{\rho}[(\bar{u}-c)\hat{w}' - \bar{u}'\hat{w}]\}' - \frac{\bar{\rho}'g}{\bar{u}-c}\hat{w} - \bar{\rho}\alpha^2(\bar{u}-c)\hat{w} = 0. \tag{4.1}$$

One or more waves can exist at a material interface located at $z = z_i$. This interface arises due to discontinuity in the base state vorticity and/or base state density. In each layer (fluid between two consecutive interfaces), both (2.3) and (4.1) are reduced to $\bar{\rho}(\bar{u}-c)[\hat{w}''-\alpha^2\hat{w}] = 0$. The discrete eigenspectrum can be obtained by assuming $(\bar{u}-c) \neq 0$, giving:

$$\hat{w}'' - \alpha^2\hat{w} = 0. \tag{4.2}$$

To ensure that there are no gaps in the continuum, the continuity of vertical velocity across an interface is imposed:

$$[\![\, \hat{w} \,]\!] = 0. \tag{4.3}$$

Here $[\![.]\!]$ denotes the limits across the interface. Continuity of pressure across the interface is ensured by the dynamic condition. Dynamic condition can be obtained by integrating (4.1) across the interface from $z_i - \Delta z$ to $z_i + \Delta z$ and letting $\Delta z \to 0$,

$$[\![\, \bar{\rho}[(\bar{u}-c)\hat{w}' - \bar{u}'\hat{w} - \frac{g\hat{w}}{\bar{u}-c}] \,]\!] = 0. \tag{4.4}$$

To capture the essence of the base state profiles given in (3.1) and (3.2), the corresponding broken-line base state velocity and density profiles are given in the following

equations. They are schematically shown in figure 9(a).

$$\bar{u}(z) = \begin{cases} U & \dfrac{z}{h} \geqslant 1, \\ \dfrac{Uz}{h} & 1 \geqslant \dfrac{z}{h} \geqslant -1, \\ -U & -1 \geqslant \dfrac{z}{h} \geqslant -h_r, \end{cases} \tag{4.5}$$

$$\bar{\rho}(z) = \begin{cases} \rho_1 & \dfrac{z}{h} > h_r, \\ \rho_2 & h_r > \dfrac{z}{h} > 0, \\ \rho_3 & 0 > \dfrac{z}{h} > -h_r. \end{cases} \tag{4.6}$$

Base state profiles given in (4.5) and (4.6) are solved using the Boussinesq version of (2.3), which ignores the density variation in inertia term, given by $\bar{\rho}'[(\bar{u}-c)\hat{w}' - \bar{u}'\hat{w}]$. Growth rate contours corresponding to the Boussinesq free-surface case are shown in the first column of figure 10. From the discussion in §3.2 it was inferred that if shear is absent at the free-surface, then non-Boussinesq and Boussinesq would yield the same result. In other words, to demonstrate that the term T_3 in (2.2) is *zero*, we solve the base state profiles given in (4.5) and (4.6) using the complete (2.3). In this regard we solve (4.2) between two consecutive interfaces and use (4.3) and (4.4) as boundary conditions. Thereby we obtain a 6th order dispersion relation for the non-Boussinesq free-surface case, which is given by $\mathscr{D}_1(c, \alpha; J_1; J_2; h_r) = 0$. In determinant form $\mathscr{D}_1$ is written as

$$\mathscr{D}_1 = \begin{vmatrix} \mathrm{e}^{\alpha h_r}(-P_1+P_2) & \mathrm{e}^{-\alpha h_r}(P_1+P_2) & 0 & 0 & 0 & 0 \\ \mathrm{e}^{\alpha} & \mathrm{e}^{-\alpha}(-2P_1+1) & 0 & 2\mathrm{e}^{-\alpha}P_1 & 0 & 0 \\ 0 & 0 & 0 & 2\alpha c & -\dfrac{J_2}{c} & -2\alpha c - \dfrac{J_2}{c} \\ 0 & 0 & 0 & 0 & P_3 & P_4 \\ \mathrm{e}^{2\alpha} & 1 & -\mathrm{e}^{2\alpha} & -1 & 0 & 0 \\ 0 & 0 & 1 & 1 & -1 & -1 \end{vmatrix}, \tag{4.7}$$

where

$$P_1 = \alpha(1-c),\ P_2 = \frac{J_1}{(1-c)},\ P_3 = \mathrm{e}^{-\alpha}\Big(\frac{2\alpha(-1-c)\mathrm{e}^{\alpha}}{\mathrm{e}^{\alpha} - \mathrm{e}^{\alpha(2h_r-1)}} - 1\Big),$$
$$P_4 = \mathrm{e}^{\alpha}\Big(\frac{2\alpha(-1-c)\mathrm{e}^{\alpha(2h_r-1)}}{\mathrm{e}^{\alpha} - \mathrm{e}^{\alpha(2h_r-1)}} - 1\Big).$$

Since $\rho_1 \ll \rho_2$ and $\rho_2 \approx \rho_3$ we have

$$J_1 = \frac{\rho_2 - \rho_1}{\rho_2 + \rho_1}\frac{gh}{U^2} \approx \frac{gh}{U^2},\ \ J_2 = \frac{2(\rho_3 - \rho_2)}{\rho_3 + \rho_2}\frac{gh}{U^2} \approx \frac{\rho_3 - \rho_2}{\rho_2}\frac{gh}{U^2}.$$

The dispersion relation $\mathscr{D}_1 = 0$ is 6th order due to the presence of six waves in the system, namely two vorticity waves (each present at a vorticity jump), two surface-gravity waves (present at the free-surface) and two interfacial-gravity waves (present at the pycnocline). The dispersion relation is solved using the inbuilt MATLAB routine 'roots'. Growth rate contours for the non-Boussinesq free-surface case are shown in the second column of figure 10. If $T_3 = 0$ (which is our inference), then the first and second

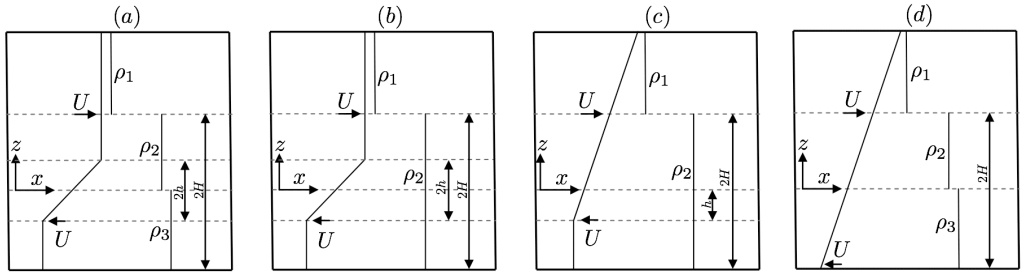

Figure 9: Base state velocity and density plots for the broken-line profiles. (a) Boussinesq/non-Boussinesq free-surface case. (b) Rayleigh free-surface model. (c) Reduced order SGLV model. (d) Reduced order SGIG model.

columns of figure 10 should be exactly the same. However we observe small differences. We have investigated the cause of this anomaly and found that it arises solely because of the definition of reference density, ρ_0. The non-Boussinesq formulation does not require a reference density, ρ_0 (which is the mean of the base state density $\bar{\rho}$). The Boussinesq formulation does require a reference density, which is taken to be the mean of the densities of air, warm water and cold water (i.e. $\rho_0 \approx 667\,\mathrm{kg/m^3}$). If we were to take the reference density for the Boussinesq case as the mean of the densities of warm water and cold water (i.e. $\rho_0 \approx 1000\,\mathrm{kg/m^3}$), then the first and second columns of figure 10 would become identical.

One important objective behind performing broken-line analysis is to find qualitative as well as quantitative agreement with the corresponding smooth profile. Comparison between third column of figure 3 with the second column of figure 10 clearly shows that the broken-line profile thoroughly captures the essence of different types of instabilities existing in the system. The quantitative agreement between smooth and broken-line profiles can be observed by comparing table 1 with table 2.

The presence of six waves in the system makes it difficult to pinpoint the mechanisms leading to each type of instability. This motivated us to construct simplified or reduced order models having lesser number of waves. Since SGLV is a new kind of instability and the mechanism leading to its formation is not yet fully understood, a reduced order set-up is constructed that has a Rayleigh type velocity profile and a free-surface. This implies that the pycnocline, and therefore the two interfacial gravity waves, have been removed from the system. This profile has been studied by both Longuet-Higgins (1998) and Bakas & Ioannou (2009), and is given in figure 9(b). We have termed this model as the "Rayleigh free-surface" model. The base velocity and density profiles are as follows:

$$\bar{u}(z) = \begin{cases} U & \dfrac{z}{h} \geqslant 1, \\ \dfrac{Uz}{h} & 1 \geqslant \dfrac{z}{h} \geqslant -1, \\ -U & -1 \geqslant \dfrac{z}{h} \geqslant -h_r, \end{cases} \tag{4.8}$$

$$\bar{\rho}(z) = \begin{cases} \rho_1 & \dfrac{z}{h} > h_r, \\ \rho_2 & h_r > \dfrac{z}{h} > -h_r. \end{cases} \tag{4.9}$$

Following a procedure similar to the non-Boussinesq free-surface case a dispersion relation $\mathscr{D}_2(c,\alpha;J_1;h_r)=0$ can be obtained for the Rayleigh free-surface model. This dispersion relation is 4th order (due to presence of four waves in the system), and is obtained by evaluating the following determinant and equating it to zero:

$$\mathscr{D}_2=\begin{vmatrix} \mathrm{e}^{\alpha h_r}(-P_1+P_2) & \mathrm{e}^{-\alpha h_r}(P_1+P_2) & 0 & 0 & 0 \\ \mathrm{e}^{\alpha} & \mathrm{e}^{-\alpha}(-2P_1+1) & 0 & 2\mathrm{e}^{-\alpha}P_1 & 0 \\ 0 & 0 & 0 & -P_5 & P_5+P_6 \\ \mathrm{e}^{2\alpha} & 1 & -\mathrm{e}^{2\alpha} & -1 & 0 \\ 0 & 0 & -\mathrm{e}^{-\alpha} & -\mathrm{e}^{\alpha} & -P_6 \end{vmatrix}. \tag{4.10}$$

Here $P_5=2\mathrm{e}^{\alpha}\alpha(-1-c)$, $P_6=\mathrm{e}^{\alpha(2h_r-1)}-\mathrm{e}^{\alpha}$. Contours of constant growth rate for varying h_r are plotted in third column of figure 10. To have parity between the different growth rate contours of figure 10, we have plotted the Rayleigh free-surface model in $\alpha-J_2$ plane. The Rayleigh free-surface model has no J_2 inherently (since there is no pycnocline), but we can scale J_1 by At to yield J_2. For large values of J_2, the third column of figure 10 reveals that the Rayleigh free-surface model very closely resembles Rayleigh/KH instability. The SGLV branch of instability arising from the non-Boussinesq free-surface case as well as the Rayleigh free-surface model are qualitatively and quantitatively similar. This implies that the interfacial gravity waves do not play any role in the SGLV mode. This mode has also been observed by Longuet-Higgins (1998) and Bakas & Ioannou (2009). From the previous literature it is not clear exactly what leads to the formation of SGLV mode, i.e. which waves play the central role in this instability. Based on the intuitive understanding of resonant interactions between counter-propagating waves, we argue that *only two* waves are essential for SGLV instability, the leftward moving surface gravity wave (wave-2 in figure 1) and the rightward moving vorticity wave (wave-6) existing at the lower vorticity interface.

To prove the above-mentioned hypothesis as well as to gain a deeper understanding behind the formation of SGLV mode, we have constructed a further reduced order model that consists only of two oppositely propagating surface gravity waves and a rightward propagating vorticity wave. We call this the SGLV model; see figure 9(c). Base state profile for this model is given below:

$$\bar{u}(z)=\begin{cases} \dfrac{2U}{h_r+1}\left(\dfrac{z}{h}\right)-\dfrac{U(h_r-1)}{h_r+1} & \dfrac{z}{h}\geqslant -1, \\ \dfrac{Uz}{h} & -1\geqslant\dfrac{z}{h}\geqslant -h_r. \end{cases} \tag{4.11}$$

$$\bar{\rho}(z)=\begin{cases} \rho_1 & \dfrac{z}{h}>h_r, \\ \rho_2 & h_r>\dfrac{z}{h}>-h_r. \end{cases} \tag{4.12}$$

The dispersion relation $\mathscr{D}_3(c,\alpha;J_1;h_r)=0$ is obtained by equating the following determinant to zero:

$$\mathscr{D}_3=\begin{vmatrix} \mathrm{e}^{\alpha h_r}(-P_1+P_2+P_7) & \mathrm{e}^{-\alpha h_r}(P_1+P_2+P_7) \\ P_3+\mathrm{e}^{-\alpha}(1-P_7) & P_4+\mathrm{e}^{\alpha}(1-P_7) \end{vmatrix}, \tag{4.13}$$

where $P_7=2/h_r+1$. It is a 3rd order equation due to presence of 3 waves in the system. To have the same Doppler shift as in the Rayleigh free-surface model, we kept the velocity at the free-surface to be U. A consequence of keeping the same Doppler shift is that the

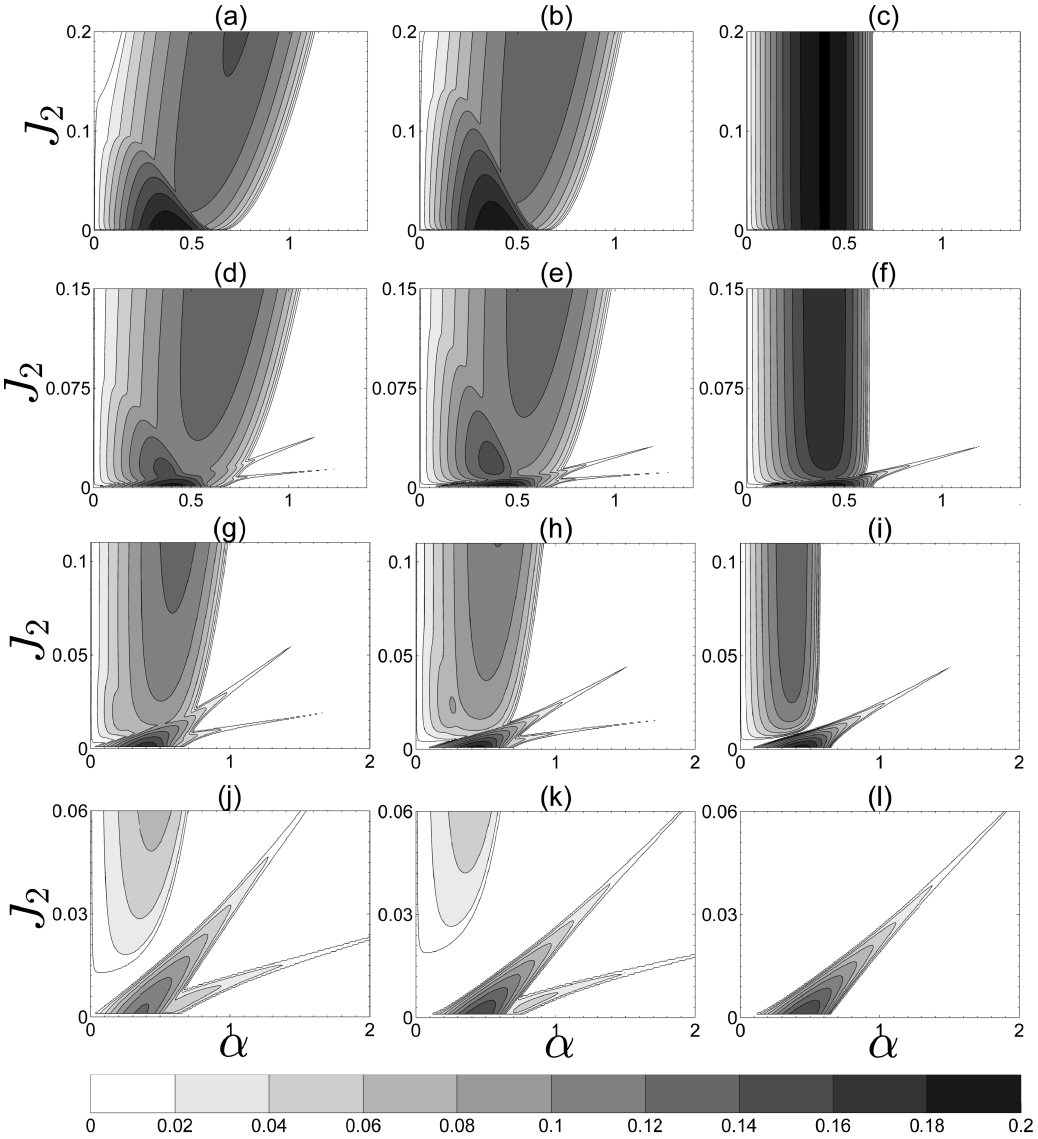

Figure 10: Growth rate contours in the $\alpha - J_2$ plane for the broken-line profiles. Each row represents growth rates for a given h_r. First row: $h_r = 10$, second row: $h_r = 4$, third row: $h_r = 3$, and fourth row: $h_r = 2$. The left, middle and right columns respectively correspond to, Boussinesq free-surface, non-Boussinesq free-surface and Rayleigh free-surface.

shear in the system changes, hence the growth rates also change since they depend on the shear scale. For comparison, and to keep a parity with the growth rates of the Rayleigh free-surface model, we have scaled the growth rates of SGLV model accordingly. Like the Rayleigh free-surface model, J_1 has been scaled by At in the reduced order SGLV model in order to get an equivalent J_2. This would maintain parity between different growth rate contours. we have plotted the growth rate contours for $h_r = 2$ in figure 11(c). A comparison between non-Boussinesq free-surface, Rayleigh free-surface model

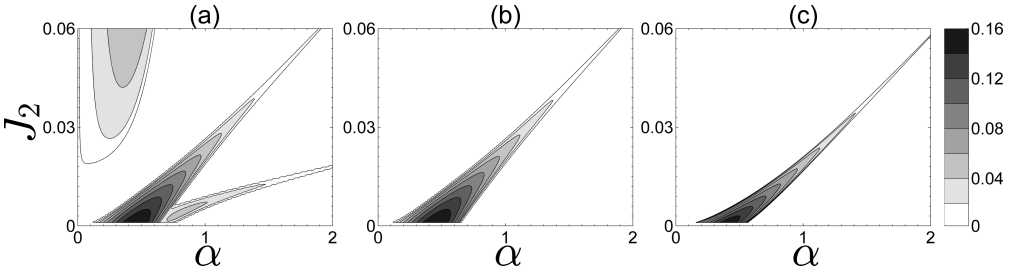

Figure 11: Growth rate contours for $h_r = 2$ case for (a) non-Boussinesq free-surface, (b) Rayleigh profile with free-surface and (c) reduced order SGLV model containing a free-surface and a lower vorticity jump.

and SGLV model for $h_r = 2$ can be made form figure 11. The SGLV mode is more prominent for lower h_r values, hence $h_r = 2$ case has been plotted. Growth rates and stability boundaries of the SGLV model qualitatively as well as quantitatively agree with both the Rayleigh free-surface and the non-Boussinesq free-surface cases. This clearly establishes that SGLV results because of interaction between the waves 2 and 6.

A small but important point worth mentioning is that there is a non-zero shear at the free-surface in the SGLV model. This shear term would modify the characteristics of the surface gravity waves (Ehrnström & Villari 2008). This is the main reason behind the minor qualitative differences between the Rayleigh free-surface model (figure 11(b)) and the SGLV model (figure 11(c)).

Apart from SGLV mode, there is yet another instability mode that is only apparent in the broken-line profile. This is the second narrow branch observed near $\alpha = 1$ and $J_2 = 0.01$ in the figure 10(k). We have termed it as the "surface gravity interfacial gravity" (SGIG) mode. To understand and isolate the essential features of this mode, another reduced order model has been constructed. The base state profiles for the reduced order SGIG model are given below (and also shown in figure 9(d)):

$$\bar{u}(z) = \frac{U}{h_r}\left(\frac{z}{h}\right) \tag{4.14}$$

$$\bar{\rho}(z) = \begin{cases} \rho_1 & \dfrac{z}{h} > h_r, \\ \rho_2 & h_r > \dfrac{z}{h} > 0, \\ \rho_3 & 0 > \dfrac{z}{h} > -h_r. \end{cases} \tag{4.15}$$

The dispersion relation for the SGIG model is given by $\mathscr{D}_4(c, \alpha; J_1; J_2; h_r) = 0$, and is obtained by equating the determinant given below to zero:

$$\mathscr{D}_4 = \begin{vmatrix} \mathrm{e}^{\alpha h_r}(-P_1 + P_2 + \dfrac{1}{h_r}) & \mathrm{e}^{-\alpha h_r}(P_1 + P_2 + + \dfrac{1}{h_r}) \\ -P_8 - \dfrac{J_2}{c} & -P_8\mathrm{e}^{2\alpha h_r} - \dfrac{J_2}{c} \end{vmatrix}, \tag{4.16}$$

where $P_8 = 2\alpha c/(1 - \mathrm{e}^{2\alpha h_r})$. Four waves are present in the SGIG model - two surface gravity waves and two interfacial gravity waves, hence $\mathscr{D}_4 = 0$ is a fourth order relation. Base state shear in the non-Boussinesq free-surface case is different from the SGIG model.

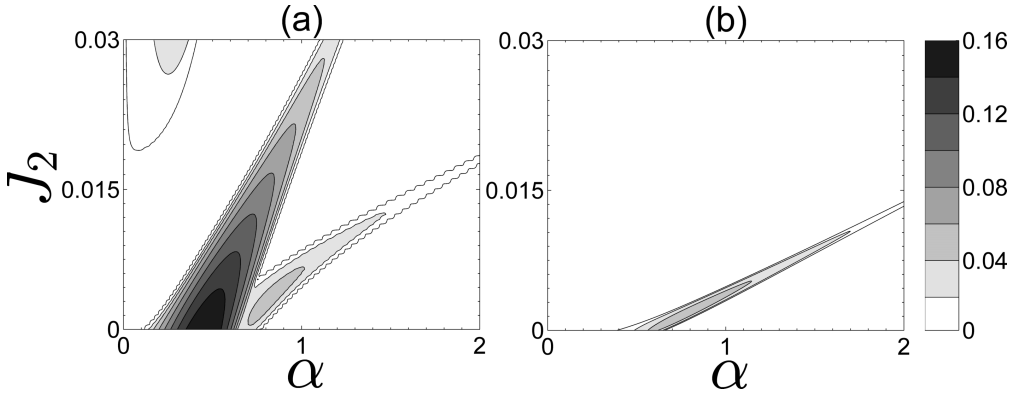

Figure 12: Contours of constant growth rate in the α-J_2 plane for $h_r = 2$, depicting the SGIG mode for (a) non-Boussinesq free-surface and (b) reduced order SGIG model that can only support surface gravity waves and interfacial gravity waves.

We have chosen an appropriate shear scale for the SGIG model, Thus, for a numerical comparison of growth rates with the non-Boussinesq free-surface case, we have scaled the SGIG model growth rates accordingly. Figure 12 shows the growth rate contours for the case of non-Boussinesq free-surface and SGIG model for $h_r = 2$. The SGIG branch of the non-Boussinesq free-surface case and the reduced order SGIG model are in qualitative and quantitative agreement. Some small differences arise because shear is present at the free-surface in the reduced order SGIG model (just like the SGLV model). We can thus conclude that the branch in the non-Boussinesq free-surface case (figure 10(k)) that occurs near $J_2 = 0.01$ and $\alpha = 1$ is due to the interaction between counter propagating surface gravity wave and interfacial gravity wave (i.e. waves $2 - 4$ of figure 1).

4.2. *Dispersion diagrams*

A standard approach to understanding shear instabilities is via dispersion diagrams (Craik 1988), which is followed here to focus on the two new types of instability, viz. SGLV and SGIG. The dispersion diagrams of SGLV and SGIG models are respectively plotted in figures 13 and 14. The dark lines correspond to the solutions of each dispersion relation ($\mathscr{D}_3 = 0$ for SGLV and $\mathscr{D}_4 = 0$ for SGIG); the imaginary part of the frequency (ω_i, which signifies the growth rate) is shown in figures 13(a) and 14(a), while the real part (ω_r) is shown in figures 13(b) and 14(b). For a given α, there should be n roots (signifying n waves) as demanded by the dispersion relation. For SGLV model $n = 3$ while for SGIG model, $n = 4$. Figure 13(b) reveals that there are 3 distinct ω_r values corresponding to each α, except for the range $0.16 < \alpha < 0.56$. In this range, two roots coalesce into one. In fact, as α increases from 0, two constituent waves come close together and coalesce at $\alpha = 0.16$, and then bifurcate into two waves at $\alpha = 0.56$. A pair of complex conjugate roots (growing and decaying normal modes) then become a possible solution; and its presence is verified from figure 13(a). The dispersion diagram obtained by solving the Rayleigh free-surface model would produce similar dispersion diagram (obviously, the number of curves would be different because SGLV has lesser roots/waves), as can be found in Longuet-Higgins (1998) and Bakas & Ioannou (2009). The instability observed is referred to as "branch II instability" by these authors.

The entire procedure applied to the SGLV model can also be applied to understand the dispersion diagrams of the SGIG model given in figures 14(a)-(b). Furthermore, the understanding obtained from the dispersion diagrams (both SGLV and SGIG) can

Case	h_r	Mode	α	J_2	γ	c_r
Boussinesq free-surface	10	KH	0.3973	0	0.20	0
	10	H	0.7965	0.2699	0.1422	$\pm$0.4691
	4	SGLV	0.4053	0	0.1885	$-$0.0504
	4	SGIG	0.7404	0.007	0.0317	0.1453
	4	KH	0.3693	0.0125	0.1458	$-$0.0132
	4	H	0.8195	0.2864	0.1415	$\pm$0.4812
	3	SGLV	0.4003	0	0.1719	$-$0.1165
	3	SGIG	0.7344	0.0065	0.0461	0.1197
	3	KH	0.2472	0.0175	0.0768	0.0045
	3	H	0.8505	0.3268	0.1389	$\pm$0.5075
	2	SGLV	0.3593	0	0.1241	$-$0.2959
	2	SGIG	0.6794	0.0045	0.0505	0.0742
	2	H	0.9675	0.5112	0.1251	$\pm$0.6014
Non-Boussinesq free-surface	10	KH	0.3973	0	0.20	$-$0.001
	10	H	0.7975	0.3973	0.1422	$\pm$0.4667
	4	SGLV	0.4163	0	0.1954	$-$0.0942
	4	SGIG	0.7004	0.0045	0.0435	0.1106
	4	KH	0.3713	0.0185	0.1480	0
	4	H	0.8235	0.4388	0.1415	$\pm$0.4844
	3	SGLV	0.4313	0	0.1880	$-$0.1945
	3	SGIG	0.7064	0.004	0.0507	0.0730
	3	KH	0.2662	0.023	0.0814	0.0128
	3	H	0.8565	0.4947	0.1389	$\pm$0.5091
	2	SGLV	0.4573	0	0.1597	$-$0.3980
	2	SGIG	0.8425	0.005	0.0466	0.0532
	2	H	0.9655	0.7616	0.1251	$\pm$0.6003
Rayleigh with free-surface	10	R	0.4003	all	0.2011	$-$0.00088
	4	R	0.4043	0.3228	0.1793	0
	4	SGLV	0.4163	0	0.1961	$-$0.0937
	3	R	0.3813	0.9790	0.1436	0
	3	SGLV	0.4303	0	0.1886	$-$0.1946
	2	SGLV	0.4553	0	0.1600	$-$0.40
SGLV model	2	SGLV	0.4161	0	0.1542	$-$0.5751
SGIG model	2	SGIG	0.7716	0.0026	0.0505	0.0394

Table 2: Growth rates and phase speeds for the maximum growth rate mode of the broken-line profiles.

be augmented by adding the dispersion relations of individual waves in isolation. The location where two isolated waves cross each other in the $\alpha - \omega_r$ plane signifies the resonant condition (i.e. waves have the same ω_r, which, to be noted, is the Doppler-shifted frequency). The dispersion relations of the isolated waves are plotted in thin black lines in figures 13(b) and 14(b). Focusing on SGLV, the dispersion relation of the isolated lower vorticity wave after appropriate Doppler shift is given by (Sutherland 2010):

$$\mathcal{V}^+ : \omega = -\alpha + \frac{2/3}{1 + \coth(\alpha)}. \tag{4.17}$$

Similarly, the dispersion relation for the isolated surface gravity waves affected by linear shear after appropriate Doppler shift is given by (Ehrnström & Villari 2008):

$$\mathcal{SG}_I{}^{\pm} : \omega = \alpha - \frac{1}{3}\tanh(4\alpha) \pm \sqrt{\Big(\frac{1}{3}\tanh(4\alpha)\Big)^2 + J_1 \alpha \tanh(4\alpha)}. \tag{4.18}$$

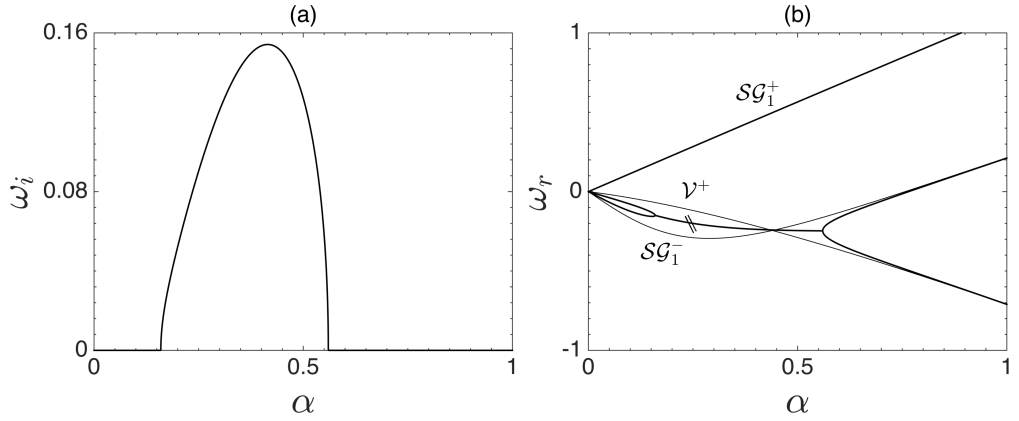

Figure 13: Dispersion diagram for the reduced order SGLV model for $J_2 = 0$ (which corresponds to the maximum growth rate case). (a) Growth rate of the unstable mode. (b) Real frequency, indicated by dark lines, are obtained by solving $\mathscr{D}_3 = 0$. The instability region is marked by two small parallel lines. The lighter lines represent the real frequencies associated with the isolated stable waves. The real frequencies of isolated waves cross near the point of maximum growth rate.

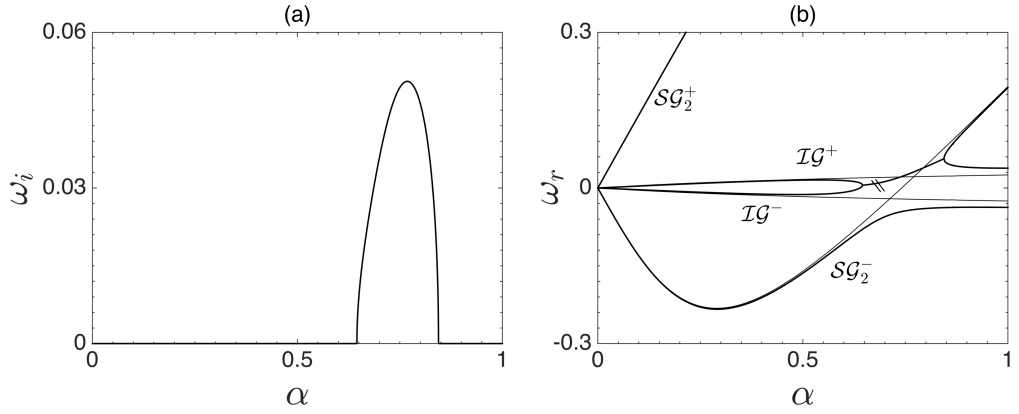

Figure 14: Same as figure 13 but for the reduced order SGIG model (here $J_2 = 0.0026$).

The two dispersion curves, $\mathcal{V}^+$ (rightward vorticity wave) and $\mathcal{SG}_1{}^-$ (leftward surface gravity wave) cross near $\alpha = 0.41$, which basically corresponds to the maximum growth rate, as can be clearly seen from figure 13(a). For large values of α, the isolated dispersion curves asymptote to the dispersion curves obtained from solving $\mathscr{D}_3 = 0$. We note here that solutions of $\mathscr{D}_3 = 0$ give ω_r of interacting waves. Since eigenfunction of a wave decays exponentially, interaction is nearly zero when α is large. Hence for large α, each curve in the dispersion diagram basically represents an isolated wave. The fast neutral mode obtained from $\mathscr{D}_3 = 0$ does not interact with any other waves in the system. It follows very closely the dispersion relation of the isolated rightward surface gravity wave, $\mathcal{SG}_1{}^+$.

Similar to the SGLV model, the instability arising in the SGIG model for $0.64 < \alpha < 0.84$ can also be understood in terms of interacting waves in isolation. To demonstrate that the SGIG mode arises due to the interaction between a surface gravity wave and an interfacial gravity wave, we consider them in isolation and plot their dispersion relations

with thin lines in figure 14(b). The dispersion relation for the stable isolated interfacial gravity waves is given below (Sutherland 2010):

$$\mathcal{IG}^{\pm} : \omega = \pm\sqrt{\frac{AtJ_1\alpha}{2\big(1+\coth(2\alpha)\big)}}. \tag{4.19}$$

For stable isolated surface gravity waves in presence of shear, the dispersion relation is given by (Ehrnström & Villari 2008):

$$\mathcal{SG}_2{}^{\pm} : \omega = \alpha - \frac{1}{4}\tanh(4\alpha) \pm \sqrt{\Big(\frac{1}{4}\tanh(4\alpha)\Big)^2 + J_1\alpha\tanh(4\alpha)}. \tag{4.20}$$

The isolated waves $\mathcal{SG}_2{}^{-}$ (leftward surface gravity wave) and $\mathcal{IG}^{+}$ (rightward interfacial gravity wave) intersect at $\alpha \approx 0.77$ in figure 14(b), which corresponds to maximum growth rate of the unstable mode in figure 14(a). The fast neutral mode obtained from the dispersion relation matches very closely with the isolated rightward surface gravity wave, $\mathcal{SG}_2{}^{+}$, which does not interact with any other wave in the system.

From figure 14(b) it can be seen that the dispersion relations of isolated leftward surface gravity wave and isolated leftward interfacial gravity wave also intersect. This intersection does not lead to an exponential instability because the intrinsic phase speeds of leftward surface gravity wave and leftward interfacial gravity wave are not opposite to each other. Wave interaction theory requires that the intrinsic phase speeds of exponentially growing waves have to be in opposing direction (Heifetz & Methven 2005; Carpenter *et al.* 2011; Guha & Lawrence 2014).

5. Discussions and Conclusions

In this paper we have considered the effects of the vertical extent of the domain and the free-surface on the stratified shear instabilities of the fluid below. In the existing literature it is customary to replace the free-surface by a rigid-lid, thereby simplifying the problem under Boussinesq approximation. However, free-surface is more than just a boundary condition because it supports two surface gravity waves. Since shear instabilities arise from resonant wave interactions, it is possible for the surface gravity waves to resonantly interact with the other waves present in the stratified shear layer (e.g. vorticity waves and interfacial gravity waves). This may modify the existing instabilities, and furthermore, can lead to new instabilities. By controlling the vertical height of the domain, the free-surface can be brought closer to the shear layer, making the coupling more feasible. To approach the problem without making any major approximations, we have developed a code that solves the non-Boussinesq Taylor-Goldstein equation. This has allowed us to capture both the strong density jump between air and water (at the free-surface)†, as well as the weak density jump between lighter and heavier water (at the pycnocline). Numerical linear stability analysis is performed on smooth base state velocity and density profiles, respectively given in (3.1) and (3.2).

First we have studied the simpler case when the free-surface is replaced by a rigid-lid, but the non-dimensional vertical height of the domain, h_r, is varied. Our results are in agreement with similar previous studies by Hazel (1972) and Haigh & Lawrence (1999). The maximum growth rate of the KH instability decreases significantly on reducing h_r - from 0.19 to 0.096 on reducing h_r from 10 to 2. However, as predicted by Haigh &

† We mention in §3.2 that the air-water free-surface can still be modeled using "Boussinesq approximation" by neglecting the non-Boussinesq baroclinic torque T_3. However caution is advised since $T_3 \neq 0$ when shear is present at the free-surface (especially true for small h_r values).

Lawrence (1999), Holmboe instability is little affected by changes in h_r. If rigid-lid approximation is not implemented, i.e. the air-water interface is treated as a non-Boussinesq free-surface, the stability boundaries are found to change drastically on decreasing h_r. Only for large values of h_r rigid-lid becomes a valid approximation since in this scenario the free-surface has practically no effect on the shear layer. Hence we infer that rigid-lid approximation is somewhat misleading and therefore should be applied with caution.

For higher values of h_r, the most unstable mode (for all bulk Richardson numbers) is due to the Rayleigh/KH instability, which arises from the coupling between two vorticity waves, each existing at an extrema of the base vorticity gradient (for broken-line profiles, this would translate to the jump in the base vorticity profile). However, as h_r is decreased, a new mode of instability appears. This mode, which we refer to as the SGLV mode, becomes the most unstable one, even surpassing KH. In fact, for very low values of h_r, KH is nearly non-existent, and the dominant instability is due to SGLV; see table 1. We note here that similar instability has been observed by Longuet-Higgins (1998) and Bakas & Ioannou (2009) while using broken-line profiles. Holmboe instability is found to be quite resilient to variations in h_r, similar to what observed in the rigid-lid case. Hence it can be concluded that rigid-lid is a valid approximation even for shallow domains if one is only interested in studying Holmboe instability.

The eigenfunction analysis performed in §3.5 reveals that Holmboe instability is analogous to the baroclinic mode in two-layered flows - the surface and interface are π shifted in phase, and furthermore, the surface elevation is insignificant in comparison to that of the interface. This is probably the reason why Holmboe instability is relatively unaffected by variations in h_r. The leftward propagating Holmboe mode is more dominant; it cusps into the lower fluid as revealed in the perturbations density contours - figures 5 and 8. The SGLV mode, on the other hand, is analogous to the barotropic mode in two-layered flows - the surface and interface (pycnocline) are nearly in phase, and the interface elevation is insignificant in comparison to that of the surface. This also implies that the pycnocline plays an insignificant role in this instability.

To complement the numerical stability analysis of the smooth profiles, and furthermore, to obtain a simplified understanding of the instabilities in the system, we have also performed stability analyses of broken-line profiles. A qualitative as well as quantitative agreement between the stability analysis of smooth and broken-line profiles is observed; compare figure 3 with 10 and table 1 with 2. The SGLV mode is clearly observed as a distinct branch of instability which arises as h_r is decreased (i.e. the depth is made shallower). An additional type of instability is observed in the broken-line profile that is hidden in the analysis of smooth profile (we refer to it as the SGIG mode). Like SGLV, the SGIG instability is also observed when the depth is quite shallow (e.g. $h_r \lesssim 4$). The broken-line profile paved the idea to construct a few reduced order broken-line models so as to underpin the wave interactions that lead to different instabilities. We have constructed three reduced order models, viz. Rayleigh with free-surface, SGLV and SGIG; see figure 9.

Through the reduced order SGLV model we have conclusively shown that the SGLV mode arises primarily because of the interaction between the leftward propagating surface gravity wave and the rightward propagating vorticity wave, i.e. interaction of waves $2-6$ of figure 1. The understanding is augmented by studying the dispersion diagrams of the full system, as well as the stable isolated waves that are suspected to be behind these instabilities. The crossing of the dispersion curves of the isolated stable waves in the $\alpha-\omega_r$ corresponds to the unstable region in the $\alpha-\omega_i$ plane, confirming our initial assumption. We emphasize here that, although this mode of instability has been observed previously by Longuet-Higgins (1998) and Bakas & Ioannou (2009), the fundamental reason behind

it was not clearly known. Neither it was known whether such instabilities exist in smooth profiles, and if yes, then how well does it compare with broken-line counterpart. In this paper we have been able to address all these points conclusively.

An approach similar to SGLV is taken to understand the SGIG mode. A reduced order SGIG model is constructed to underpin the instability mechanism. Finally, with the help of dispersion diagrams, we confirmed that the SGIG mode is indeed an interaction of the leftward surface gravity wave (wave-2) and rightward interfacial gravity wave (wave-4). This mode, to the best of our knowledge, has not been previously reported in the literature.

In summary, we have performed a comprehensive study on the effect of free-surface on the stratified shear instabilities below. For shallow flows, i.e., when the free-surface is relatively closer to the shear layer, the free-surface significantly affects the ensuing shear instabilities. The surface gravity waves couple with the different waves constituting the shear layer, thereby modifying the "well-known" instabilities, and more importantly, giving rise to two new instabilities. Future experimental studies and/or Direct numerical simulation (DNS) may be able to shed more light into these instabilities, especially their non-linear evolution and three dimensional structures. Another possible future extension of this work would be to consider the "no-wind" case. Our preliminary results in this direction show similarity with the current work, but presence of new modes is a possibility.

Appendix A. Derivation of Non-Boussinesq Taylor-Goldstein Equation

A full derivation of the non-Boussinesq viscous diffusive Taylor-Goldstein equation is given here. A 2D flow in the x-z plane is considered. The horizontal, x component of velocity is given by u while the vertical, z component of velocity is given by w. The dynamic viscosity and mass density of fluid are given by μ and ρ respectively. Acceleration due to gravity is given by g, while t denotes time. The governing equations of the problem are given below.

Incompressible continuity equation:

$$\frac{\partial u}{\partial x} + \frac{\partial w}{\partial z} = 0. \tag{A 1}$$

Navier-stokes equation for x-momentum:

$$\rho\Big(\frac{\partial u}{\partial t} + u\frac{\partial u}{\partial x} + w\frac{\partial u}{\partial z}\Big) = -\frac{\partial p}{\partial x} + \mu\Big(\frac{\partial^2 u}{\partial x^2} + \frac{\partial^2 u}{\partial z^2}\Big). \tag{A 2}$$

Navier-stokes equation for z-momentum:

$$\rho\Big(\frac{\partial w}{\partial t} + u\frac{\partial w}{\partial x} + w\frac{\partial w}{\partial z}\Big) = -\frac{\partial p}{\partial z} - \rho g + \mu\Big(\frac{\partial^2 w}{\partial x^2} + \frac{\partial^2 w}{\partial z^2}\Big). \tag{A 3}$$

Advection diffusion of the stratifying agent:

$$\frac{\partial \theta}{\partial t} + u\frac{\partial \theta}{\partial x} + w\frac{\partial \theta}{\partial z} = \eta\Big(\frac{\partial^2 \theta}{\partial x^2} + \frac{\partial^2 \theta}{\partial z^2}\Big). \tag{A 4}$$

Equation of state relating stratifying agent to density:

$$\rho = \rho_0[1 - \gamma(\theta - \theta_0)]. \tag{A 5}$$

In equations (A 4) and (A 5), θ is the stratifying agent like temperature or salinity, η is the molecular diffusivity of the stratifying agent, while γ is the linear coefficient relating density to changes in stratifying agent. Also ρ_0 and θ_0 are the base state density and

some reference value of the stratifying agent concentration. Combining equations (A 4) and (A 5) we obtain an advection diffusion equation for mass density given by

$$\frac{\partial \rho}{\partial t} + u\frac{\partial \rho}{\partial x} + w\frac{\partial \rho}{\partial z} = \kappa\Big(\frac{\partial^2 \rho}{\partial x^2} + \frac{\partial^2 \rho}{\partial z^2}\Big). \tag{A 6}$$

Base states that are independent of time and dependent only on z, the vertical coordinate are considered. The base state is given by $u = \bar{u}(z)$, $w = 0$, $p = \bar{p}(z)$ and $\rho = \bar{\rho}(z)$. Hydrostatic balance is assumed for the base state given by $d\bar{p}/dz = -\bar{\rho}g$. Perturbations to the base state are considered, given by $u = \bar{u}(z) + \tilde{u}$, $w = \tilde{w}$, $p = \bar{p}(z) + \tilde{p}$, and $\rho = \bar{\rho}(z) + \tilde{\rho}$. Perturbation quantities are denoted by $\tilde{f}$, where f is a placeholder variable. The perturbed base state is substituted in (A 1)-(A 3), and (A 6) to yield:

$$\frac{\partial \tilde{u}}{\partial x} + \frac{\partial \tilde{w}}{\partial z} = 0, \tag{A 7}$$

$$(\tilde{\rho} + \bar{\rho})\Big(\frac{\partial \tilde{u}}{\partial t} + \tilde{u}\frac{\partial \tilde{u}}{\partial x} + \bar{u}\frac{\partial \tilde{u}}{\partial x} + \tilde{w}\frac{\partial \tilde{u}}{\partial z} + \tilde{w}\frac{d\bar{u}}{dz}\Big) = -\frac{\partial \tilde{p}}{\partial x} + \mu\Big(\frac{\partial^2 \tilde{u}}{\partial x^2} + \frac{\partial^2 \tilde{u}}{\partial z^2}\Big), \tag{A 8}$$

$$(\tilde{\rho} + \bar{\rho})\Big(\frac{\partial \tilde{w}}{\partial t} + \tilde{u}\frac{\partial \tilde{w}}{\partial x} + \bar{u}\frac{\partial \tilde{w}}{\partial x} + \tilde{w}\frac{\partial \tilde{w}}{\partial z}\Big) = -\frac{\partial \tilde{p}}{\partial z} - \frac{\partial \bar{p}}{\partial z} - \tilde{\rho}g - \bar{\rho}g + \mu\Big(\frac{\partial^2 \tilde{w}}{\partial x^2} + \frac{\partial^2 \tilde{w}}{\partial z^2}\Big), \tag{A 9}$$

$$\frac{\partial \tilde{\rho}}{\partial t} + \tilde{u}\frac{\partial \tilde{\rho}}{\partial x} + \bar{u}\frac{\partial \tilde{\rho}}{\partial x} + \tilde{w}\frac{\partial \tilde{\rho}}{\partial z} + \tilde{w}\frac{d\bar{\rho}}{dz} = \kappa\Big(\frac{\partial^2 \tilde{\rho}}{\partial x^2} + \frac{\partial^2 \tilde{\rho}}{\partial z^2}\Big). \tag{A 10}$$

Only the linear terms in (A 7)-(A 10) are retained, by making the assumption that perturbations infinitesimal.

$$\frac{\partial \tilde{u}}{\partial x} + \frac{\partial \tilde{w}}{\partial z} = 0, \tag{A 11}$$

$$\bar{\rho}(\frac{\partial \tilde{u}}{\partial t} + \bar{u}\frac{\partial \tilde{u}}{\partial x} + \tilde{w}\frac{d\bar{u}}{dz}) = -\frac{\partial \tilde{p}}{\partial x} + \mu\Big(\frac{\partial^2 \tilde{u}}{\partial x^2} + \frac{\partial^2 \tilde{u}}{\partial z^2}\Big), \tag{A 12}$$

$$\bar{\rho}(\frac{\partial \tilde{w}}{\partial t} + \bar{u}\frac{\partial \tilde{w}}{\partial x}) = -\frac{\partial \tilde{p}}{\partial z} - \tilde{\rho}g + \mu\Big(\frac{\partial^2 \tilde{w}}{\partial x^2} + \frac{\partial^2 \tilde{w}}{\partial z^2}\Big), \tag{A 13}$$

$$\frac{\partial \tilde{\rho}}{\partial t} + \bar{u}\frac{\partial \tilde{\rho}}{\partial x} + \tilde{w}\frac{d\bar{\rho}}{dz} = \kappa\Big(\frac{\partial^2 \tilde{\rho}}{\partial x^2} + \frac{\partial^2 \tilde{\rho}}{\partial z^2}\Big). \tag{A 14}$$

We assume that the perturbations are of the normal mode form having wave like nature along the horizontal direction, x. See Drazin & Reid (2004), Charru (2011) and Schmid & Henningson (2012) for normal mode stability theory. Perturbations of the form $\tilde{f}(x, z, t) = \hat{f}(z)\mathrm{e}^{\mathrm{i}\alpha(x-ct)}$, are added in (A 11)-(A 14):

$$\mathrm{i}\alpha\hat{u} + \hat{w}' = 0, \tag{A 15}$$

$$\bar{\rho}(\mathrm{i}\alpha(\bar{u} - c)\hat{u} + \hat{w}\bar{u}') = -\mathrm{i}\alpha\hat{p} + \mu(\hat{u}'' - \alpha^2\hat{u}), \tag{A 16}$$

$$\bar{\rho}(\mathrm{i}\alpha(\bar{u} - c)\hat{w}) = -\hat{p}' - \hat{\rho}g + \mu(\hat{w}'' - \alpha^2\hat{w}), \tag{A 17}$$

$$\mathrm{i}\alpha(\bar{u} - c)\hat{\rho} + \hat{w}\bar{\rho}' = \kappa(\hat{\rho}'' - \alpha^2\hat{\rho}). \tag{A 18}$$

Making the substitution $\hat{u} = \mathrm{i}\hat{w}'/\alpha$ we get

$$\bar{\rho}[-(\bar{u} - c)\hat{w}' + \bar{u}'\hat{w}] = -\mathrm{i}\alpha\hat{p} + \frac{\mathrm{i}}{\alpha}\mu[\hat{w}''' - \alpha^2\hat{w}'].$$

Total derivative of the above mentioned equation with respect to z yields:

$$\bar{\rho}'[-(\bar{u}-c)\hat{w}'+\bar{u}'\hat{w}]+\bar{\rho}[-\bar{u}'\hat{w}'-(\bar{u}-c)\hat{w}''+\bar{u}''\hat{w}+\bar{u}'\hat{w}'] = -\mathrm{i}\alpha\hat{p}'+\frac{\mathrm{i}}{\alpha}\mu[\hat{w}''''-\alpha^2\hat{w}'']. \quad (A\,19)$$

Expressing $\hat{p}'$ in terms of other variables from (A 17) we get:

$$\hat{p}' = -\mathrm{i}\bar{\rho}\hat{w}\alpha(\bar{u}-c) - \hat{\rho}g + \mu(\hat{w}''-\alpha^2\hat{w}).$$

$\hat{p}'$ from the previous equation can be substituted in (A 19) to give:

$$\bar{\rho}'[-(\bar{u}-c)\hat{w}'+\bar{u}'\hat{w}]+\bar{\rho}[-(\bar{u}-c)\hat{w}''+\alpha^2(\bar{u}-c)\hat{w}+\bar{u}''\hat{w}] = \mathrm{i}\alpha\hat{\rho}g+\frac{\mathrm{i}}{\alpha}\mu[\hat{w}''''-2\alpha^2\hat{w}''+\alpha^4\hat{w}], \quad (A\,20)$$

$$\mathrm{i}\alpha(\bar{u}-c)\hat{\rho}+\hat{w}\bar{\rho}' = \kappa(\hat{\rho}''-\alpha^2\hat{\rho}). \quad (A\,21)$$

Equations (A 20) and (A 21), form the *non-Boussinesq viscous diffusive Taylor-Goldstein equations*. Inviscid limit gives rise to $\mu \to 0$, while the non-diffusive limit yields $\kappa \to 0$. In the limiting condition that the flow becomes inviscid and non-diffusive we get:

$$\bar{\rho}'[-(\bar{u}-c)\hat{w}'+\bar{u}'\hat{w}]+\bar{\rho}[-(\bar{u}-c)\hat{w}''+\alpha^2(\bar{u}-c)\hat{w}+\bar{u}''\hat{w}] = \mathrm{i}\alpha\hat{\rho}g, \quad (A\,22)$$

$$\mathrm{i}\alpha(\bar{u}-c)\hat{\rho}+\hat{w}\bar{\rho}' = 0. \quad (A\,23)$$

Combining (A 22) and (A 23) we get:

$$\bar{\rho}'\Big[(\bar{u}-c)\hat{w}'-\bar{u}'\hat{w}-\frac{g}{\bar{u}-c}\hat{w}\Big]+\bar{\rho}\Big[(\bar{u}-c)(\hat{w}''-\alpha^2\hat{w})-\bar{u}''\hat{w}\Big] = 0. \quad (A\,24)$$

The *non-Boussinesq Taylor-Goldstein equation* is given by (A 24), that is similar to the non-Boussinesq equation obtained by Barros & Choi (2011), Barros & Choi (2014) and Carpenter *et al.* (Accepted).

REFERENCES

Alexakis, A. 2005 On Holmboe's instability for smooth shear and density profiles. *Phys. Fluids* **17** (8), 084103.

Baines, P. G. & Mitsudera, H. 1994 On the mechanism of shear flow instabilities. *J. Fluid Mech.* **276**, 327–342.

Bakas, N. A. & Ioannou, P. J. 2009 Modal and nonmodal growths of inviscid planar perturbations in shear flows with a free surface. *Phys. Fluids* **21** (2), 024102.

Barros, R. & Choi, W. 2011 Holmboe instability in non-Boussinesq fluids. *Phys. Fluids* **23** (12), 124103.

Barros, R. & Choi, W. 2014 Elementary stratified flows with stability at low Richardson number. *Phys. Fluids* **26** (12), 124107.

Carpenter, J. R., Balmforth, N. J. & Lawrence, G. A. 2010 Identifying unstable modes in stratified shear layers. *Phys. Fluids* **22** (5), 054104.

Carpenter, J. R., Guha, A. & Heifetz, E. Accepted A physical interpretation of the wind-wave instability as interacting waves. *J. Phys. Oceanogr* .

Carpenter, J. R., Lawrence, G. A. & Smyth, W. D. 2007 Evolution and mixing of asymmetric Holmboe instabilities. *J. Fluid Mech.* **582**, 103–132.

Carpenter, J. R., Tedford, E. W., Heifetz, E. & Lawrence, G. A. 2011 Instability in stratified shear flow: Review of a physical interpretation based on interacting waves. *Appl. Mech. Rev.* **64** (6), 060801 1–17.

Carpenter, J. R., Tedford, E. W., Heifetz, E. & Lawrence, G. A. 2013 Instability in stratified shear flow: Review of a physical interpretation based on interacting waves. *Appl. Mech. Rev.* **64** (6), 060801–17.

Caulfield, C-C. P. 1994 Multiple linear instability of layered stratified shear flow. *J. Fluid Mech.* **258**, 255–285.

Charru, F. 2011 *Hydrodynamic Instabilities*. Cambridge University Press.

Craik, A. D. D. 1988 *Wave interactions and fluid flows*. Cambridge University Press.

Drazin, P.G. 2002 *Introduction to Hydrodynamic Stability*. Cambridge University Press.

Drazin, P. G. & Reid, W. H. 2004 *Hydrodynamic stability*. Cambridge university press.

Ehrnström, M. & Villari, G. 2008 Linear water waves with vorticity: rotational features and particle paths. *J. Diff. Eqs.* **244** (8), 1888–1909.

Guha, A. & Lawrence, G. A. 2014 A wave interaction approach to studying non-modal homogeneous and stratified shear instabilities. *J. Fluid Mech.* **755**, 336–364.

Guha, A., Rahmani, M. & Lawrence, G. A. 2013 Evolution of a barotropic shear layer into elliptical vortices. *Phys. Rev. E* **87** (1), 013020.

Haigh, S. P. & Lawrence, G. A. 1999 Symmetric and nonsymmetric Holmboe instabilities in an inviscid flow. *Phys. Fluids* **11** (6), 1459–1468.

Hazel, P. 1972 Numerical studies of the stability of inviscid stratified shear flows. *J. Fluid Mech.* **51** (01), 39–61.

Heifetz, E., Bishop, C. H. & Alpert, P. 1999 Counter-propagating Rossby waves in the barotropic Rayleigh model of shear instability. *Q. J. R. Meteorol. Soc.* **125** (560), 2835–2853.

Heifetz, E. & Mak, J. 2015 Stratified shear flow instabilities in the non-Boussinesq regime. *Phys. Fluids* **27** (8), 086601.

Heifetz, E. & Methven, J. 2005 Relating optimal growth to counterpropagating Rossby waves in shear instability. *Phys. Fluids* **17** (6), 064107.

Holmboe, J. 1962 On the behavior of symmetric waves in stratified shear layers. *Geophys. Publ* **24**, 67–113.

Lawrence, G. A., Browand, F. K. & Redekopp, L. G. 1991 The stability of a sheared density interface. *Phys. Fluids* **3**, 2360–2370.

Longuet-Higgins, M. S. 1998 Instabilities of a horizontal shear flow with a free surface. *J. Fluid Mech.* **364**, 147–162.

Miles, J. W. 1957 On the generation of surface waves by shear flows. *J. Fluid Mech.* **3** (02), 185–204.

Rahmani, M., Lawrence, G. A. & Seymour, B. R. 2014 The effect of Reynolds number on mixing in Kelvin–Helmholtz billows. *J. Fluid Mech.* **759**, 612–641.

Sakai, S. 1989 Rossby-Kelvin instability: a new type of ageostrophic instability caused by a resonance between Rossby waves and gravity waves. *J. Fluid Mech.* **202**, 149–176.

Schmid, P.J. & Henningson, D.S. 2012 *Stability and Transition in Shear Flows*. Springer New York.

Shete, M. H. & Guha, A. 2016 On a new non-boussinesq instability in stratified lakes and oceans. *arXiv preprint arXiv:1610.08385* .

Smyth, W. D., Carpenter, J. R. & Lawrence, G. A. 2007 Mixing in symmetric Holmboe waves. *J. Phys. Oceanogr* **37** (6), 1566–1583.

Smyth, W. D., Klaassen, G. P. & Peltier, W. R. 1988 Finite amplitude Holmboe waves. *Geophys. Astrophys. Fluid* **43** (2), 181–222.

Smyth, W. D., Moum, J. N. & Nash, J. D. 2011 Narrowband oscillations in the upper equatorial ocean. Part II: Properties of shear instabilities. *J. Phys. Oceanogr.* **41** (3), 412–428.

Smyth, W. D. & Peltier, W. R. 1989 The transition between Kelvin-Helmholtz and Holmboe instability: an investigation of the overreflection hypothesis. *J. Atmos. Sci.* **46** (24), 3698–3720.

Smyth, W. D. & Peltier, W. R. 1991 Instability and transition in finite-amplitude Kelvin–Helmholtz and Holmboe waves. *J. Fluid Mech.* **228**, 387–415.

Sutherland, B. R. 2010 *Internal gravity waves*. Cambridge University Press.

Sutherland, B. R. & Peltier, W. R. 1992 The stability of stratified jets. *Geophys. Astrophys. Fluid* **66** (1-4), 101–131.

Turner, J. S. 1979 *Buoyancy effects in fluids*. Cambridge University Press.

Yoshida, S., Ohtani, M., Nishida, S. & Linden, P. F. 1998 Mixing processes in a highly stratified river. *Physical Processes in Lakes and Oceans* pp. 389–400.